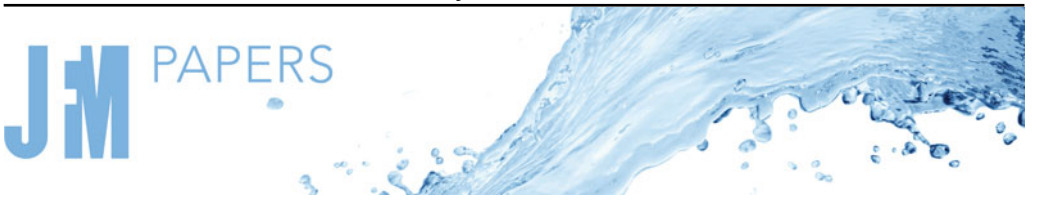
J. Fluid Mech. (2026), *vol.* 1034, A9, doi:10.1017/jfm.2026.11461



Finite-time mixing and reaction in packed-bed reactors

Dario Maggiolo[1], **Lucien Magson**[2,3], **Gunther Munz**[4], **Diego Sampedro**[2] and **Angela Sasic Kalagasidis**[5]

[1]Department of Mechanical Engineering, Chalmers University of Technology, Göteborg 41296, Sweden

[2]Departamento de Química, Instituto de Investigación Química de la Universidad de La Rioja, C/Madre de Dios 53, Logroño, La Rioja 26006, Spain

[3]French Alternative Energies and Atomic Energy Commission, Saclay / Siège, 91191 Gif-sur-Yvette CEDEX, France

[4]Heating and Cooling Technologies, Fraunhofer Institute for Solar Energy Systems (ISE), Heidenhofstrase 2, Freiburg 79110, Germany

[5]Department of Architecture and Civil Engineering, Chalmers University of Technology, Göteborg 41296, Sweden

Corresponding author: Dario Maggiolo, maggiolo@chalmers.se

(Received 28 September 2024; revised 13 March 2026; accepted 18 March 2026)

We investigate mixing dynamics in porous media at finite times, using pore-scale lattice-Boltzmann simulations combined with Lagrangian particle tracking. We compute fluid deformation in randomly packed beds based on the moving Protean frame approach introduced by Lester *et al.* (2018 *J. Fluid Mech.* 855, 770–803). From the extracted Lagrangian kinematics, we construct a mixing model based on lamellar aggregation that well predicts the Eulerian scalar fields obtained from simulations. Our results reveal an early-time mixing regime dominated by shear-driven fluid deformation, where solute mixing arises from the random overlap of diffusive concentration elements. In this regime, mixing proceeds slowly and follows a temporal decay of concentration variance, $\sigma_c^2 \propto Pe^{-\alpha/(2\alpha+1)}t^{-1/2}$, where Pe is the Péclet number and α the exponent characterising shear deformation. This dynamic arises when the Péclet number is small relative to the ratio between the exponential-mixing and shear-deformation time scales. This analysis also demonstrates that shear-induced mixing governs the homogenisation of early-stage reactions at the fluid–solid interface in finite-size random packed beds, typically operating at moderate Péclet numbers $Pe = O(10^2)$.

Key words: porous media, laminar mixing, reacting multiphase flow

© The Author(s), 2026. Published by Cambridge University Press. This is an Open Access article, distributed under the terms of the Creative Commons Attribution licence (https://creativecommons.org/licenses/by/4.0/), which permits unrestricted re-use, distribution and reproduction, provided the original article is properly cited.

https://doi.org/10.1017/jfm.2026.11461 Published online by Cambridge University Press

1. Introduction

Although fully developed mixing in porous media has been widely studied, the dynamics of mixing at early, finite times remains less well understood.

In porous systems of limited size or characterised by finite-time processes such as reactions, finite-time mixing plays a decisive role in controlling the homogenisation of an injected solution. Consider, for instance, small compact porous reactors: in such systems, while molecular diffusion is too slow to support mixing, pore-scale advection contributes to distributing the solute effectively within the limits of the reactor's longitudinal size L. Nevertheless, the residence time L/U has to be long enough to allow complete molecular conversion (Maggiolo *et al.* 2020), implying that the device must operate at a limited mean flow velocity U and Péclet number. As a result, advection-driven mixing is weak and constrained by the limited physical reactor space L.

Limited-size porous systems are also encountered in a range of other applications, such as membranes and electrodes (Farzaneh *et al.* 2021). Furthermore, in highly reactive media, mixing may be limited at very short times, because species transport is subsequently inhibited by reaction. Under such conditions, fully developed mixing may not be achieved and the mixing dynamics is fully realised at finite times.

Whether because of a fast reaction time or a physically short medium, the time available for solute mixing may be shorter than the characteristic mixing time t_m that marks the onset of asymptotic behaviour. This mixing time scales proportionally to the characteristic pore length d and inversely to the mean flow velocity, $t_m \propto d/U$. More precisely, t_m reflects the specific kinematic mechanisms of mixing dictated by the pore-scale flow and geometry.

At finite or large Péclet numbers, solutes transported through porous media often organise into thin, high-concentration filaments separated by low-concentration voids (Dentz & de Barros 2015). Mixing refers to the transition of a scalar field – such as concentration – from an initially heterogeneous, segregated state to a final, spatially homogeneous distribution (Villermaux 2019). In porous media, this process relies on the ability of the flow to eliminate small-scale concentration contrasts through kinematic deformations generated by the pore-scale geometry at very early times. In other words, mixing is completely mediated by the pore-scale architecture.

Unlike two-dimensional flows, three-dimensional porous structures inherently generate chaotic flow (Lester *et al.* 2013, 2016), where random sequences of stretching and folding events produce long-term exponential stretching of concentration fields (Heyman *et al.* 2020). The average long-term growth rate of infinitesimal fluid element lengths is quantified by the Lyapunov exponent, λ, which determines the onset of chaotic mixing at $t_m \sim d/(2\lambda U)\ln(Pe)$. Turuban *et al.* (2019) further demonstrated that chaotic mixing in granular porous media with simple artificial lattice structures – although weaker than in non-granular open pore networks – depends strongly on the orientation of the mean flow relative to the lattice geometry. For the specific case of random stretching orientations, the Lyapunov exponent has been theoretically estimated as $\lambda \approx 0.11$ (Lester *et al.* 2013, 2016). Experimental studies in random packed beds report slightly higher values: $\lambda = 0.20$ (Kree & Villermaux 2017), $\lambda = 0.21$ (Heyman *et al.* 2020) and $\lambda = 0.17$ (Heyman *et al.* 2021).

In the presence of fast reaction times, or if the porous bed physical length is limited to only a few grain diameters, there is insufficient time for fully developed mixing, since the residence time $1/k_r$ or L/U with k_r the reaction rate, respectively, becomes comparable to the mixing time $d/(\lambda U)$. The Lyapunov exponent is an infinite-time measure and

https://doi.org/10.1017/jfm.2026.11461 Published online by Cambridge University Press

does not fully capture the three-dimensional deformation. At such short times, shear-induced deformation and chaotic mixing coexist. Lester *et al.* (2018) showed that, at finite times, shear-induced deformation may dominate. Heyman *et al.* (2021) documented the emergence of chaotic mixing signatures only after an initial transient phase, during which concentration differences persist. This transient phase is consistent with the fact that chaotic mixing requires time to fully develop (at least the time needed to reach the Batchelor scale corresponding to the exponential mode of mixing). Aquino *et al.* (2023) showed how shear deformation governs the long-time distribution of species in porous media and the statistics of travel times to solid reactive surfaces, effectively determining the reaction efficiency of the porous medium. However, the transient regime leading to this asymptotic limit remains insufficiently explored.

Lamellar theories have been developed to capture this dynamics. Initially proposed for turbulent flows (Duplat & Villermaux 2008) and later extended to random porous flows (Dentz, Hidalgo & Lester 2023), these models describe mixing as the formation of elongated lamellae (or sheets) of high concentration and their subsequent random aggregation. This framework highlights an early stretching–compression regime, during which advection (i) redistributes regions of high concentration randomly in space, bringing previously segregated pockets into proximity, and (ii) amplifies transverse concentration gradients within lamellae, thereby accelerating diffusion-driven dilution. Both processes act as powerful mixing mechanisms. After t_m, the overlapping lamellae can be modelled as undergoing random aggregation, either fully or partially correlated depending on the pore-scale dynamics (Duplat, Jouary & Villermaux 2010; Heyman *et al.* 2024).

The lamellar model thus provides a useful framework for studying finite-time mixing, as it also captures the early-time fluid-induced deformation kinematics. This kinematics depend on several factors, most notably (i) the spatial dimensionality of the stirring protocol and (ii) the distribution and randomness of the flow. Villermaux (2019) reviews various stirring protocols, including the two-dimensional shear-induced deformation. For this case, the predictive accuracy of lamellar theory has been experimentally validated (Souzy *et al.* 2018), and the mixing time has been shown to exhibit a weak algebraic dependence on the Péclet number, scaling as $t_m \sim (d/U)Pe^{1/3}$. A similar scaling applies to shear-induced mixing by a vortex (Villermaux 2019).

In the present work, we quantitatively investigate the finite-time behaviour of mixing in monodisperse packed beds using computational analyses within both Eulerian and Lagrangian frameworks.

The research questions we address are: (i) which mixing mode is most relevant at finite times in packed-bed porous media; (ii) how this mixing mode affects the pore-scale concentration distribution at the fluid–solid interface; and (iii) whether the homogeneity of surface reactions in finite-size packed-bed reactors can be modelled and predicted. From a fundamental perspective, addressing these questions is essential to advancing the understanding of early-time mixing in porous media. From a technological perspective, new models are required to capture the early-time redistribution of species at fluid–solid interfaces within packed beds, thereby improving the design and operational control of small-scale porous reactors.

Two numerical approaches are commonly proposed to quantify pore-scale mixing and to extract the corresponding macroscopic reaction rates. Eulerian models track the temporal evolution of concentration fields (Gurung & Ginn 2020), whereas Lagrangian approaches, such as random reactive walks (Valocchi, Bolster & Werth 2019; Sole-Mari *et al.* 2021), follow individual tracer trajectories. Both approaches face computational challenges: Eulerian models require high-resolution pore-scale discretisation, while Lagrangian models are constrained by the number of tracers that can be resolved. Other modelling

https://doi.org/10.1017/jfm.2026.11461 Published online by Cambridge University Press

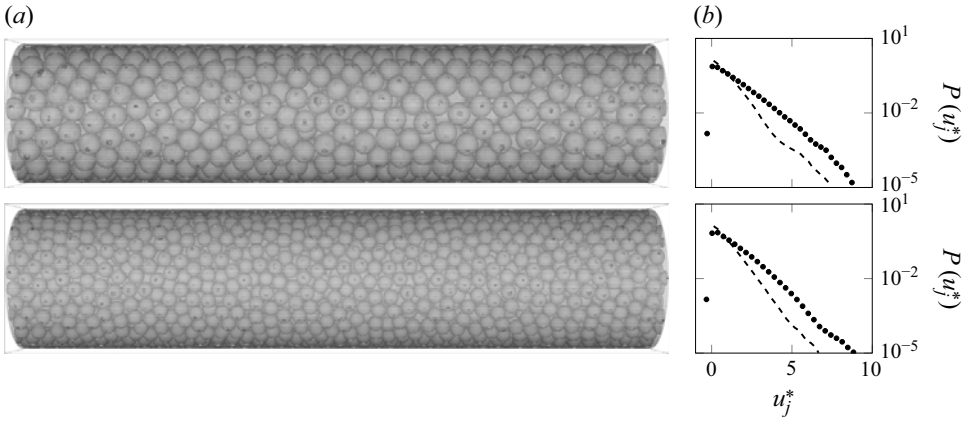


Figure 1. (*a*) Two tubular reactors of radius R containing reactive porous media composed of catalyst spherical particles of size $d = R/3.1$ (upper panel) and $d = R/4.7$ (lower panel). The two systems are used as geometrical input for the lattice-Boltzmann simulations. (*b*) Probability distribution functions of normalised flow velocities $u_j^*(\boldsymbol{x}) = u_j(\boldsymbol{x})/U$ (with U the mean streamwise flow velocity) along the streamwise u_x (black marks) and transverse $u_t = (u_y^2 + u_z^2)^{1/2}$ (dashed line) directions; particles of size $d = R/3.1$ (upper panel) and $d = R/4.7$ (lower panel).

frameworks, including fractal derivative diffusion models (Liang *et al.* 2023) and effective reactive transport equations (Dentz, Gouze & Carrera 2011), can be used to account for heterogeneity, anomalous diffusion and small-scale mixing. However, these models rely on microstructural parameters describing the pore geometry, which are often difficult to measure *a priori*, making direct pore-scale simulations indispensable.

To solve the Eulerian flow and concentration fields at the pore scale we use the lattice-Boltzmann methodology (LBM), which is well suited for solving laminar flows in a complex geometry, since it allows an easy local representation of the pore surfaces projected onto a regular spatial grid. We consider as a test case the geometry of a packed bed contained in tubular channels of finite length. We then apply a Lagrangian particle tracking (LPT) algorithm to calculate the Lagrangian trajectories of massless particles (tracers) advected by the flow. Along these trajectories, we compute the deformation tensor, based on the moving Protean framework of Lester *et al.* (2018), which ultimately allows us to determine the dominant modes of fluid-induced deformation at finite times. We then employ a lamellar model constructed over the computed deformations to predict the spatial reorganisation and mixing of regions of varying concentration. We assess the validity of the lamellar model by comparing its predictions with the solution of the Eulerian concentration field.

The paper is organised as follows: § 2 describes the numerical methodology, §§ 3.1 and 3.2 investigate the characteristics of pore-scale velocities and deformations, § 3.3 and § 3.4 analyse the evolution of the concentration fields, whereas §§ 3.5 and 3.6 interpret the mixing dynamics using a lamellar aggregation model, which we will then extend to reactive porous systems in § 3.8. § 4 concludes with a summary of the main findings.

2. Numerical methodology

2.1. *Geometry construction*

To study finite-time mixing, we take a small fixed packed bed as an example: quasi-spherical catalytic particles are close packed into a tubular reactor (figure 1). A molecular

https://doi.org/10.1017/jfm.2026.11461 Published online by Cambridge University Press

solution is continuously injected, while the catalyst particle surfaces trigger chemical reactions that progressively convert the solute. A notable example is Molecular Solar Thermal Energy Storage (MOST) Systems, where light-activated molecules store solar energy in the form of chemical bonds (Wang *et al.* 2019; Magson *et al.* 2024). The solute concentration is typically kept low to prevent molecular inhibition, while the porous geometry of the packed bed provides a high specific surface area for reactions. The choice of a small reactor size offers advantages such as (i) efficient energy extraction, (ii) reduced catalyst use and maintenance and (iii) compact integration into small containers. These systems are highly sensitive to mixing evolution at the pore scale. Indeed, assuming fully developed mixing and a rapid development of well-mixed conditions can lead to significant errors in predicting reactor performance (Sole-Mari, Bolster & Fernàndez-Garcia 2023).

We construct the reactor geometry using the open-source computer graphics software tool Blender. The rigid-body dynamics of spherical particles falling into a cylindrical container is simulated to mimic the microstructure of catalyst reactors composed of spherical particles. We consider two geometrical configurations, with reactor radius to particle diameter ratios of $R/d = 3.1$ and 4.7. The reactor lengths are scaled accordingly, with $L = 28d$ and $42d$.

After particle deposition, we extract the particle centre positions and reconstruct binarised three-dimensional image matrices of the resulting geometries. These binarised images contain 7.5 10^7 and 13.1 10^8 voxels, with voxel-to-particle size ratios of $\Delta x/d \approx 1/40$ and $\Delta x/d \approx 1/32$ for the $R/d = 3.1$ and 4.7 configurations, respectively. This resolution ensures that the voxel size, later used for the numerical lattice-Boltzmann computation, remains smaller than the smallest characteristic transport scale relevant to the targeted flow velocity (Batchelor length scale under linear shear $s_b/d \sim Pe^{-1/3} \approx 1/7$, under exponential stretching in packed beds $s_b/d \sim (0.1Pe)^{-1/2} \approx 1/5$, see also § 3.6). The two configurations are shown in figure 1, panel (*a*).

2.2. *Pore-scale simulations*

The LBM is applied to solve the momentum equation and solute reaction at the pore scale. The LBM is particularly well suited for this task due to its ease of algorithmic parallelisation, enabling efficient numerical solvers on high-performance computing infrastructures, including flows in complex geometries. We use the open-source code lbdm (Maggiolo 2024), which has previously been applied to model solute transport and reactions in porous media. Validation of this algorithm for porous medium applications is provided e.g. in Maggiolo, Modin & Kalagasidis (2023).

The momentum equation is first solved within the porous geometry by computing the streaming and collision of a lattice population driven by a body force that mimics a pressure gradient. Two buffer zones of length R are added at the inlet and outlet of the catalyst section. These are extensions of the reactor container without obstacles, allowing streamwise realignment of the flow and enabling periodic boundary conditions. This strategy allows the application of a body force mimicking a pressure gradient, avoiding the manipulation of boundary pressures and improving the numerical stability Yang & Wang (2023). At the fluid–solid boundaries, no-slip conditions are imposed. After steady state is reached, the flow Péclet number is $Pe = Ud/D_m \approx 280$ in all simulations, U being the mean flow velocity and D_m the molecular diffusivity. At this value of Pe, chaotic mixing features are expected to emerge (Lester, Metcalfe & Rudman 2014).

The flow field is solved via a single-relaxation-time lattice-Boltzmann equation

$$f_r(\boldsymbol{x} + \boldsymbol{c}_r, t+1) - f_r(\boldsymbol{x}, t) = -\tau_\nu^{-1}\big(f_r(\boldsymbol{x}, t) - f_r^{eq}(\boldsymbol{x}, t)\big) + F_r, \tag{2.1}$$

https://doi.org/10.1017/jfm.2026.11461 Published online by Cambridge University Press

where $f_r(\boldsymbol{x}, t)$ is the distribution function at the position $\boldsymbol{x} = (x, y, z)$ and time t along the rth direction, $\boldsymbol{c}_r$ is the discrete velocity vector along the rth direction and τ_v is the relaxation time (proportional to fluid viscosity). With f_r^{eq} we indicate the equilibrium distribution function along the rth direction

$$f_r^{eq}(\boldsymbol{x}, t) = w_r \rho \left(1 + \frac{c_{rj} u_j(\boldsymbol{x}, t)}{c_s^2} + \frac{(c_{rj} u_j(\boldsymbol{x}, t))^2}{c_s^4} - \frac{u_j^2(\boldsymbol{x}, t)}{2c_s^2}\right), \tag{2.2}$$

where c_s is the speed of sound and w_r the three-dimensional 19-speed lattice weight parameter of the three-dimensional lattice structure along the rth direction. The fluid field is computed in each computational cell by integrating the hydrodynamic moments of the distribution functions. The steady-state velocity vector $u_j(\boldsymbol{x})$, and density $\rho(\boldsymbol{x})$ are then obtained as

$$\rho(\boldsymbol{x}) = \sum_r f_r(\boldsymbol{x}), \tag{2.3}$$

$$\rho(\boldsymbol{x}) u_j(\boldsymbol{x}) = \sum_r c_{rj} f_r(\boldsymbol{x}) + \frac{1}{2}\left(\frac{\Delta P}{L}\right)_j. \tag{2.4}$$

Here, $\Delta P/L$ is the applied pressure gradient that drives the fluid through the medium. This term also appears in the body force F_r in (2.1) as (Guo, Zheng & Shi 2002)

$$F_r(\mathbf{x}, t) = \left(1 - \frac{1}{2\tau_v}\right) w_r \left(\frac{c_{rj} - u_j(\mathbf{x}, t)}{c_s^2} + \frac{c_{rj} u_j(\mathbf{x}, t)}{c_s^4} c_{rj}\right) \left(\frac{\Delta P}{L}\right)_r. \tag{2.5}$$

In the next step, the computed steady-state flow field is used to solve the transport of a passive scalar concentration c via a second lattice population. The scalar is continuously injected at the inlet at concentration c_0 and may react at the catalyst–fluid interface.

The system is governed by the steady incompressible momentum equation

$$u_j^* \frac{\partial u_i^*(\boldsymbol{x})}{\partial x_j^*} = -\frac{\partial p^*}{\partial x_i^*} + \frac{\partial}{\partial x_j^*}\left(\frac{1}{\Re} \frac{\partial u_j^*(\boldsymbol{x})}{\partial x_j^*}\right), \tag{2.6}$$

and by the advection–diffusion–reaction equation

$$\frac{\partial c^*(\boldsymbol{x}, t)}{\partial t^*} + \frac{\partial c^*(\boldsymbol{x}, t) u_j^*(\boldsymbol{x})}{\partial x_j^*} = \frac{\partial}{\partial x_j^*}\left(\frac{1}{Pe} \frac{\partial c^*(\boldsymbol{x}, t)}{\partial x_j^*}\right), \tag{2.7}$$

where $c^*(\boldsymbol{x}, t) = c(\boldsymbol{x}, t)/c_0$ is the dimensionless concentration, $u_j^*(\boldsymbol{x}) = u_j(\boldsymbol{x})/U$ is the dimensionless velocity along the jth direction and $x_j^* = x_j/d$. We impose zero-flux boundary conditions at the container walls and outlet. The Reynolds number is set at $\Re = Ud/\nu = 0.5 < 1$ and we confirmed that inertial effects are negligible by ensuring that the pore-scale flow statistics (probability distribution functions) are the same when computed at $\Re = 0.005$ (not shown here). This result is in line with Nissan & Berkowitz (2018), who report non-negligible inertial effects from $\Re = 10$.

At the catalyst surface, denoted by the inward-pointing normal direction λ, a first-order kinetic law is applied

$$-\left.\frac{\partial c^*(\boldsymbol{x}, t)}{\partial \lambda^*}\right|_S = Da_I \, c^*(\boldsymbol{x}, t)|_S, \tag{2.8}$$

where $Da_I = k_s d/D_m$ is the pore-scale Damköhler number, relating the characteristic velocity of surface reaction k_s (in m s^{-1} units) to the pore-scale diffusive velocity D_m/d. Here, $\lambda^* = \lambda/d$ denotes the dimensionless interface normal.

https://doi.org/10.1017/jfm.2026.11461 Published online by Cambridge University Press

Case	R/d	L/d	Da_I	Da_{II}	Pe
(A1) inert	3.1	28	0	0	277
(A2) reactive	3.1	28	3.33	2	277
(B1) inert	4.7	42	0	0	274
(B2) reactive	4.7	42	2.22	2	274

Table 1. Simulated cases. The table reports the values of the reactor-to-particle size ratios, R/d and L/d. The macroscopic Damköhler number is set to $Da_{II} = k_v L/U$, with values of 0 (inert case) and 2 (reactive case). In all simulations, the Péclet number is $Pe = Ud/D_m \approx 280$, and the Reynolds number is $Re = Ud/\nu \approx 0.5$.

case	d (μm)	R (mm)	L (cm)	flow rate (ml h^{-1})	D_m (m^2 s^{-1})	k_v (s^{-1})
(A2)	833	2.5	2.3	12	10^{-9}	$3\ 10^{-2}$
(B2)	533	2.5	2.3	18	10^{-9}	$3\ 10^{-2}$

Table 2. Dimensional parameters for the two simulated reactors, cases A2 and B2 in table 1, relevant for e.g. MOST applications. Values of particle diameters and reaction rates reflect those of a typical catalyst employed, container dimensions and flow rates are comparable to those of small size miniature reactors (Magson *et al.* 2024). Molecular diffusivities correspond to typical values of hydrocarbons in liquids (Price & Söderman 2000).

For the purpose of reactor design, we define a advection-based macroscopic Damköhler number

$$Da_{II} = \frac{k_v L}{U} = \frac{k_s s_p (1-\phi)}{\phi} \frac{L}{U}, \tag{2.9}$$

which relates the macroscopic reaction rate $k_v = k_s s_p (1-\phi)/\phi$ to the mean residence time L/U, with $s_p = 6/d$ the specific surface area of the catalyst particle and $\phi \approx 0.5$ the porosity.

We examine two cases for each geometric configuration: an inert case, with $Da_{II} = 0$, and a reactive case, with $Da_{II} \approx 2$. The latter ensures that the reactor operates under mass-controlled conditions and achieves optimised conversion (Maggiolo *et al.* 2020). The relevant dimensionless parameters are summarised in table 1, whereas in table 2 we report the dimensional parameters relevant for packed-bed reactor applications, such as MOST systems.

2.3. *Lagrangian particle tracking and fluid deformation along streamlines*

We apply a LPT algorithm to study the kinematics governing fluid deformation. Indeed, fluid deformation ultimately controls the spatial distribution of scalar quantities transported by the flow, i.e. their dynamic mixing. The stationary flow field obtained from the LBM simulations is used as input to the LPT algorithm, from which Lagrangian statistics are extracted. The governing equation of LPT

$$\frac{\mathrm{d}\boldsymbol{x}(t, \boldsymbol{X})}{\mathrm{d}t} = \boldsymbol{u}[\boldsymbol{x}(t, \boldsymbol{X})] \tag{2.10}$$

is solved using a third-order Runge–Kutta method (Maggiolo, Picano & Guarnieri 2016), where $\boldsymbol{x}$ and $\boldsymbol{X}$ denote Eulerian and Lagrangian positions, respectively. We track 500 trajectories, randomly initialised at the inlet, and follow them until they reach, on average, half the length of the medium.

https://doi.org/10.1017/jfm.2026.11461 Published online by Cambridge University Press

The extracted Lagrangian statistics are used in § 3.3 to quantify macroscopic dispersion behaviour, and in § 3.2 to analyse local fluid deformation. For the latter, we employ the procedure of Lester *et al.* (2018), which involves constructing a Protean moving reference frame. For steady flows, the Protean frame is essentially a streamline frame. This transformation renders the velocity gradient tensor upper triangular, simplifying the solution of the deformation tensor, and separating stretching from shear deformations.

The transformation is expressed as two successive reorientations, $\boldsymbol{Q}(t) = \boldsymbol{Q}_1(t)\boldsymbol{Q}_2(t)$. The first reorientation, $\boldsymbol{Q}_1$, aligns the velocity vector with the Protean frame. The second, $\boldsymbol{Q}_2$, applies an arbitrary rotation about the streamline direction. A specific choice of this rotation angle, $\alpha(t)$, ensures that the velocity gradient tensor becomes upper triangular. The angle $\alpha(t)$ is obtained from an ordinary differential equation whose coefficients depend on the velocity components $v_i(t)$, with $i = 1, 2, 3$, and the velocity gradient tensor components $\epsilon_{ij}(t)$, evaluated at each time step along the Lagrangian trajectories.

The velocity components are directly available from the LPT solution for each tracer at each time step, while the velocity gradient tensor is computed via trilinear interpolation on the computational grid. Near solid surfaces, when a grid node required for interpolation lies outside the fluid domain, no-slip boundary conditions are enforced by mirroring the velocity from the nearest fluid node.

For further details on the Protean frame, we refer the reader to Lester *et al.* (2018). A derivation of the velocity gradient tensor and a validation test case are provided in Appendix A.

3. Results

3.1. *Flow topology*

We begin our analysis by characterising pore-scale velocities and deformations. Figure 1(*b*) shows the probability density functions (PDFs) of pore-scale velocities in the streamwise direction, $u_x(\boldsymbol{x})$, and in the transverse direction, $u_t(\boldsymbol{x}) = (u_y^2(\boldsymbol{x}) + u_z^2(\boldsymbol{x}))^{1/2}$. The results reveal that most high-velocity flow paths are longitudinally aligned. The difference between the streamwise and transverse velocity PDFs, which highlights this preferential streamwise alignment, depends only weakly on particle size across the investigated R/d ratios. Moreover, the velocity PDFs are nearly identical for the two transverse confinement cases, $R/d = 4.7$ and $R/d = 3.1$. This indicates that wall-induced hydrodynamic effects are minimal, and the media can effectively be considered transversely unbounded (as confirmed by the wall-to-core fluid ratios $d/2/(2R - d) < 0.1$ Ziółkowska & Ziółkowski 1988).

At the pore scale, solid obstacles combined with no-slip boundary conditions generate viscous shear, which is important for deformation of scalar concentrations as well as for regulating surface reactions (Aquino *et al.* 2023). The characteristic sizes of pore constrictions are identified using a three-dimensional Delaunay triangulation applied to the set of particle centres. This approach is well suited for spherical packings (Ben-Noah, Hidalgo & Dentz 2025). For each triangle defined by three particle centres, we compute the pore constriction area A_p, its characteristic size $\ell_p = \sqrt{A_p}$ and the unit normal vector $\boldsymbol{\eta}$. The latter is not necessarily aligned with the positive streamwise direction. Its orientation relative to the Cartesian axes (x, y, z) is quantified by the polar and azimuthal angles, θ_p and φ_p, as illustrated in figure 2(*d*).

Three main descriptors are therefore used here to characterise the statistics of pore-scale topology: (i) pore constrictions ℓ_p, (ii) streamwise alignment given by the polar angle θ_p and (iii) transverse orientation given by the azimuthal angle φ_p. The PDFs of

https://doi.org/10.1017/jfm.2026.11461 Published online by Cambridge University Press

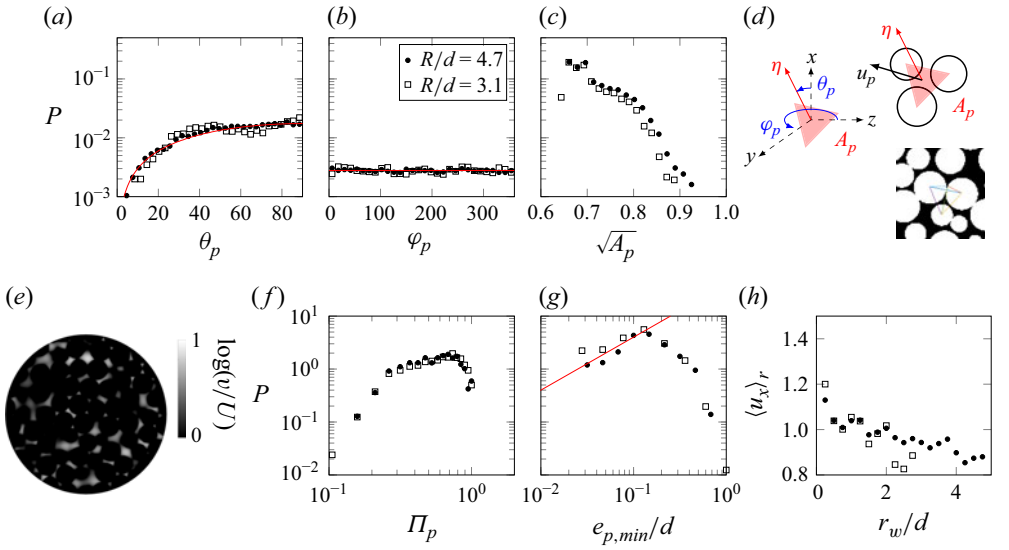


Figure 2. The PDFs of the polar (θ_p) and azimuthal (φ_p) angles of the normal vector to pore constrictions $\boldsymbol{\eta}$ (panels *a*,*b*), and the PDF of constrictions' characteristic sizes $\sqrt{A_p}$ (panel *c*), computed via Delaunay triangulation. Panel (*d*) illustrates a triangular pore constriction (top), with the associated pore-scale velocity $\boldsymbol{u}_p$ and normal $\boldsymbol{\eta}$, and shows the segmented pore space with Delaunay triangulation (bottom). Red solid lines in (*a*) and (*b*) correspond to uniform distributions of $\cos\theta_p$ and φ_p. In (*c*), the sizes of pore constrictions exhibit a narrow distribution, with $\sqrt{A_p}/d \approx 0.5 - 1$. Panel (*e*) shows a cross-section of the flow field with the dimensionless pore-scale velocity magnitude v/U displayed in logarithmic grey scale: this representation helps to assess the shape of the pore spaces, which are in large part non-circular. Panels (*f*) and (*g*) report the PDF of the ratio Π_p between minimum and maximum axes of the ellipses inscribed in the pore spaces (*f*) and the PDF of the dimensionless minimum axis $e_{p,min}/d$ (*g*). These panels confirm that pore spaces are non-circularly shaped, and that the probability of pore constrictions (small values of $e_{p,min}$, panel (*g*), red line) qualitatively scales linearly with $e_{p,min}$. In the last panel (*h*) we report the variation of the longitudinal velocity averaged over a cylindrical volume of length L and diameter $R - r_w$, where r_w is the distance from the packed-bed container walls. Wall effects are clearly visible up to $r_w/d \approx 1/2$.

θ_p and φ_p, reported in figure 2(*a*,*b*), closely follow the theoretical uniform distributions of $\cos\theta_p$ and φ_p (red lines), indicating no preferential orientation of pore-normal vectors. Pore constrictions (figure 2*c*), by contrast, show a much narrower distribution, typically ranging from $\ell_p \sim 0.5d$ to d. This randomness in orientations is expected to influence how concentrations spread and mix, as will be discussed in § 3.6.

3.2. *Lagrangian fluid deformation*

Fluid deformation arises from different mechanisms. While shear flows induce algebraic deformation (Souzy *et al.* 2018), stretching and folding processes cause exponential deformation of fluid elements in random media (Heyman *et al.* 2020). These mechanisms interplay to generate deformations as the product of a power-law and exponential functions. To quantify the relative contributions of shear-induced deformation versus exponential deformation, we compute the deformation tensor $\boldsymbol{F}'(t)$ along Lagrangian trajectories in the Protean reference frame. Identifying the dominant deformation mechanisms is essential, as they govern solute mixing and porous medium's homogenisation efficiency.

We first extract pore-scale velocity magnitudes $v = (u_i^2)^{1/2}$ along fluid trajectories, with $i = 1, 2, 3$ indicating the three Protean directions. Figures 3(*a*) and 3(*b*) display the

https://doi.org/10.1017/jfm.2026.11461 Published online by Cambridge University Press

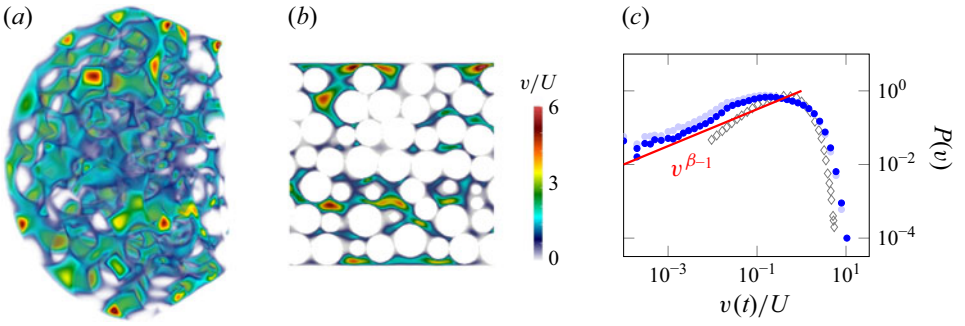


Figure 3. Eulerian velocity magnitude fields v/U on a volumetric slice (a) and on a cross-section in the (x, z) plane (b). (c) The PDF of velocities v/U sampled along Lagrangian trajectories. The exponent $\beta = 3/2$ is extracted from the low-velocity tail of the distribution using (3.1) (red line). Dark and light blue circles correspond to the cases $R/d = 4.7$ and $R/d = 3.1$, respectively, while grey diamond markers report the data from Souzy *et al.* (2020).

Eulerian velocity magnitude fields, both in a three-dimensional slice and on a symmetry plane. Sampling the dimensionless velocities v/U along Lagrangian trajectories yields the PDF shown in figure 3(c). From this distribution, we extract the power-law exponent β, assuming that low-velocity statistics follow the heavy-tailed form characteristic of heterogeneous media (Berkowitz *et al.* 2006)

$$P(v < U) \propto v^{\beta-1}. \tag{3.1}$$

This analysis gives $\beta \approx 3/2$ (red line in figure 3c). Interestingly, the low-velocity distribution is not flat, as it would be if the pore cross-sections were circular (Dentz, Icardi & Hidalgo 2018). In circular cross-sections the PDF at low velocities follows the solution of the Poiseuille flow in a pipe, where regions of low velocity (near the pipe walls) are more probable than regions of high velocity. The high probability of low-velocity regions is compensated by the low probability of low velocities in parabolic flow profiles, such as Poiseuille flows, resulting in a flat probability distribution of low velocities, i.e. $P(v < U) \propto v^0$. In non-circular cross-sections, the picture is different: in rectangular cross-sections the probability of low velocities increases with increasing velocity, because the probability of finding regions of low velocities does not continue increasing as the walls are approached (see e.g. Stewart & Zhang 2013; in the limit case of a two-dimensional flow the probability of low-velocity regions is flat). Via image segmentation performed at several cross-sections (thresholding on v/U, see figure 2e), we quantitatively discern and identify individual pore areas; we observe that pore spaces are largely non-circular and oblong, with a ratio between minimum and maximum inscribed axes $\Pi_p = e_{p,min}/e_{p,max} < 1$ and a distribution of pore constrictions scaling qualitatively as $P(e_{p,min}) \propto e_{p,min}$, see figure 3 panels ($f$) and ($g$). de Anna *et al.* (2017) showed that, for a power-law distribution of pore throats in two dimensions, the low-velocity distribution scales as a power law with an exponent that is half of the exponent of the pore-throat distribution. Our findings are consistent with this result, as the low-velocity power-law exponent in (3.1) satisfies $\beta - 1 = 1/2$. This suggests that the pore spaces are better approximated by quasi–two-dimensional geometries (with $e_{p,min}$ denoting the two-dimensional pore size), rather than by fully three-dimensional pores with circular cross-sections.

https://doi.org/10.1017/jfm.2026.11461 Published online by Cambridge University Press

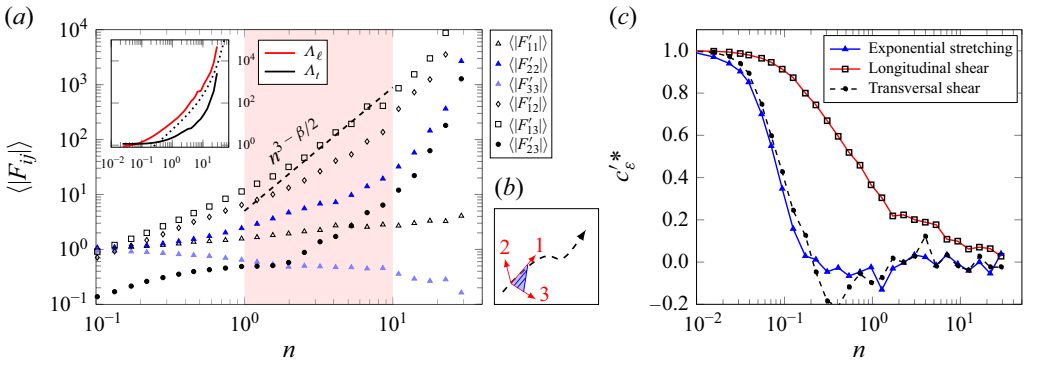


Figure 4. (*a*) Evolution of the deformation tensor components, averaged over the Lagrangian trajectories, for the case $R/d = 4.7$. Longitudinal shear-induced components F'_{12} and F'_{13} dominate at early times ($n < 10$), well captured by the prediction (3.3) (dashed lines). Inset: comparison between computed longitudinal and transverse deformations (Λ_ℓ as per (3.4), $\Lambda_t = \langle \sqrt{{F'_{22}}^2 + {F'_{33}}^2 + {F'_{23}}^2} \rangle$) and the cross-over prediction (3.6) (dotted lines). (*b*) Example of the Protean frame (red arrows) orientation with respect to a Lagrangian trajectory (black dashed line); the blued shaded area schematically represents fluid shear deformation F'_{13}. (*c*) Autocorrelation c'^*_ϵ of velocity gradient tensor components $\epsilon'_{ij}(t)$, showing long-lived correlations of shear rate components ϵ'_{12} and ϵ'_{13} (longitudinal shear) beyond a pore-scale travel time $n = 1$, compared with rapidly decorrelating transversal shear rates ϵ'_{23} and exponential rates ϵ'_{11}, ϵ'_{22}, ϵ'_{33}.

Next, we analyse the components of the deformation tensor, which reads as

$$\boldsymbol{F}'(t) = \begin{pmatrix} F'_{11}(t) & F'_{12}(t) & F'_{13}(t) \\ 0 & F'_{22}(t) & F'_{23}(t) \\ 0 & 0 & F'_{33}(t) \end{pmatrix}. \tag{3.2}$$

The off-diagonal terms $F'_{12}(t)$, $F'_{13}(t)$ and $F'_{23}(t)$, associated with deformation in the streamwise (F'_{12}, F'_{13}) and transverse (F'_{23}) directions, quantify shear deformation at finite times and the combined effect of shear and stretching at later times. The diagonal terms $F'_{11}(t)$, $F'_{22}(t)$ and $F'_{33}(t)$ capture pure compression and stretching along the Protean axes induced by velocity intermittencies. Figure 4(*a*) shows their time evolution: deformation is initially governed by shear, with F'_{12} and F'_{13} dominating up to $n \approx 10$ (red shaded region,$n = tU/d$ is the characteristic dimensionless time). At later times, exponential deformations (diagonal terms F'_{22} and F'_{33}) become comparable in magnitude and are expected to dominate at longer times (Lester *et al.* 2018). The early-time shear regime is particularly relevant in finite systems, where the macroscopic length is only a few particle diameters and reactions may occur before exponential stretching develops.

The mathematical framework of Lester *et al.* (2018) explains this behaviour. At very early times, deformation evolves ballistically; prior to exponential stretching ($t < t_\epsilon$), shear dominates. Specifically, F'_{13} follows a power law in n

$$|F'_{13}(t < t_\epsilon)| \approx \gamma_2^* n^{3-\beta/2}, \tag{3.3}$$

where γ_2^* is an effective shear rate in the (1, 3) plane of the Protean frame and β is the velocity PDF exponent. Figure 4(*a*) confirms that this model accurately captures the average deformation $\langle |F'_{13}(t)| \rangle$ (where $\langle\rangle$ indicates the averaging over the computed Lagrangian trajectories), with $\gamma_2^* \approx 5$. This value is smaller than that reported for ordered bead packs ($\gamma^* \approx 40$) (Aquino *et al.* 2023). This discrepancy is expected as ordered packs can trigger optimal mixing (Turuban *et al.* 2018, 2019). The evolution of $\langle |F'_{12}(t)| \rangle$

https://doi.org/10.1017/jfm.2026.11461 Published online by Cambridge University Press

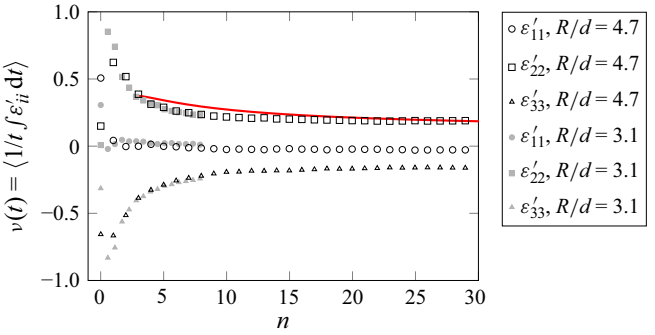


Figure 5. Finite-time Lyapunov exponent $\langle \nu(t) \rangle$: comparison between numerical estimates (markers, obtained via the finite-time solution of (3.5)) and the prediction (3.7) with $\lambda = 0.1$, $\beta = 3/2$ (red line). Grey markers: case with stronger confinement, $R/d = 3.1$.

is similar to $\langle |F'_{13}(t)| \rangle$ but slightly slower, whereas $|F'_{22}(t)| \ll |F'_{13}(t)|$, which is the main result of interest, showing that shear-induced deformation dominates at finite times. Algebraic functions (such as shear deformation) grow faster than exponential ones (stretching) at short times. However, the converse is true at long times. Hence, the switch from shear to stretching at finite times is universal. Whether one deformation mode prevails on the other to determine mixing instead depends on the specific shear intensity, as we will discuss later in § 3.7. Assuming $|F'_{12}| \sim |F'_{13}|$, the longitudinal growth of a material line at finite times is given by

$$\Lambda_\ell(t < t_\epsilon) = \left\langle \sqrt{{F'_{11}}^2(t) + {F'_{12}}^2(t) + {F'_{13}}^2(t)} \right\rangle \approx \gamma^* n^\alpha, \tag{3.4}$$

with $\alpha = 3 - \beta/2 \approx 2.25$ and an effective shear rate in three dimensions $\gamma^* = (2\gamma_2^{*2})^{1/2} \approx 5\sqrt{2}$. This scaling will later be used to model concentration aggregation and mixing.

The onset of exponential stretching occurs at the characteristic time $t_\epsilon = 1/\lambda$, where λ is the infinite-time Lyapunov exponent

$$\lambda = \left\langle \lim_{t\to\infty} \frac{1}{t} \int_0^t \epsilon'_{22}(t), \mathrm{d}t \right\rangle = -\left\langle \lim_{t\to\infty} \frac{1}{t} \int_0^t \epsilon'_{33}(t), \mathrm{d}t \right\rangle. \tag{3.5}$$

Following Lester *et al.* (2018), the cross-over between shear-induced and exponential deformation is described by

$$\Lambda_\ell(t) \approx \gamma^* n^{2-\beta/2} \exp(\lambda t), \tag{3.6}$$

while the finite-time Lyapunov exponent evolves as

$$\langle \nu(t) \rangle \approx \lambda + \left(2 - \frac{\beta}{2}\right) \frac{\ln(n)}{n}, \tag{3.7}$$

which converges to λ for $t, n \to \infty$. Numerically computing $\nu(t)$ via the solution of (3.5) at finite times and fitting with (3.7) yields $\lambda \approx 0.1$ (figure 5, markers and red line). This value agrees well with the one computed for random stretching orientations (Lester *et al.* 2016). Predictions from (3.6) (dotted line) also match the observed longitudinal deformation across the cross-over regime (figure 4 inset). Transverse deformation $\Lambda_t(t)$ should instead scale exponentially (Lester *et al.* 2018), as confirmed by our simulations (inset of figure 4*a*). Combining (3.7) with (3.3) one can directly observe the dependence

https://doi.org/10.1017/jfm.2026.11461 Published online by Cambridge University Press

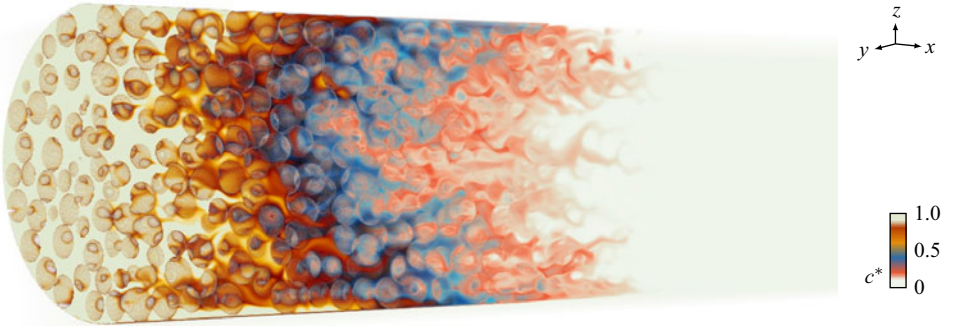


Figure 6. Snapshot of scalar transport in an inert porous reactor ($R/d = 4.7$). The dimensionless concentration $c^*(\boldsymbol{x}, t) = c(\boldsymbol{x}, t)/c_0$ is injected at the left boundary at constant concentration c_0. Filaments (or sheets) of concentration are visible near the mean front position $c^* \approx 0.5$ (blue region).

of the finite-time Lyapunov exponent on the dominant shear deformation F'_{13}

$$\langle \nu(t) \rangle \approx \lambda + \frac{1}{n}\Big[\ln\left(\gamma_2^{*-1}\left\langle F'_{13}(n)\right\rangle\right) - \ln(n)\Big]. \tag{3.8}$$

Finally, we note that the intermediate deformation regime is dominated by correlated shear events, which gradually lose correlation as the exponential regime is approached (figure 4*c*). In particular, shear-induced deformations remain correlated well beyond a pore-scale travel time ($n = 1$). The autocorrelation of velocity gradient components is computed as

$$c'^{*}_{\epsilon} = \frac{\left\langle \left(\epsilon'_{ij}(t) - \langle \epsilon'_{ij}(t)\rangle\right)\left(\epsilon'_{ij}(0) - \left\langle \epsilon'_{ij}(0)\right\rangle\right)\right\rangle}{\left\langle \left(\epsilon'_{ij}(t) - \langle \epsilon'_{ij}(t)\rangle\right)^2\right\rangle^{1/2}\left\langle \left(\epsilon'_{ij}(0) - \langle \epsilon'_{ij}(0)\rangle\right)^2\right\rangle^{1/2}}, \tag{3.9}$$

where $\epsilon'_{ij}(t)$ are components of the upper-triangular velocity gradient tensor. This correlation play a key role in controlling the randomness of scalar aggregation (Duplat *et al.* 2010), and it will be further discussed in § 3.6.

3.3. *Dispersion of tracers and evolution of the concentration front*

We now turn to the analysis of scalar dispersion and mixing. We first analyse inert porous media, before extending the discussion to reactive systems. In this section and § 3.4 we analyse dispersion and mixing from Eulerian data of pore-scale simulations, whereas in §§ 3.5, 3.6 and 3.7 we interpret the results with mixing models based on Lagrangian deformation.

When a scalar is injected into the porous reactor, flow deformation strongly influences the distribution of concentration. This effect is especially evident near the mean concentration front, i.e. close to the isosurface $c^* \approx 0.5$ (figure 6). Here, filaments of concentration emerge along high-velocity flow paths, which correspond to regions of strong deformation. More specifically, concentration sheets are formed and stretched preferentially along the dominant flow direction. The same phenomenon occurs for the complementary concentration field $c_w = 1 - c^*$, which we refer to as the white concentration elements (in contrast to the black high-concentration regions). The most prominent white regions, corresponding to low concentration, appear in the wakes of catalyst particles (figure 7*a*). In cross-section, these regions resemble two-dimensional sheets (figure 7*b*), which occasionally overlap transversely (red arrows).

https://doi.org/10.1017/jfm.2026.11461 Published online by Cambridge University Press

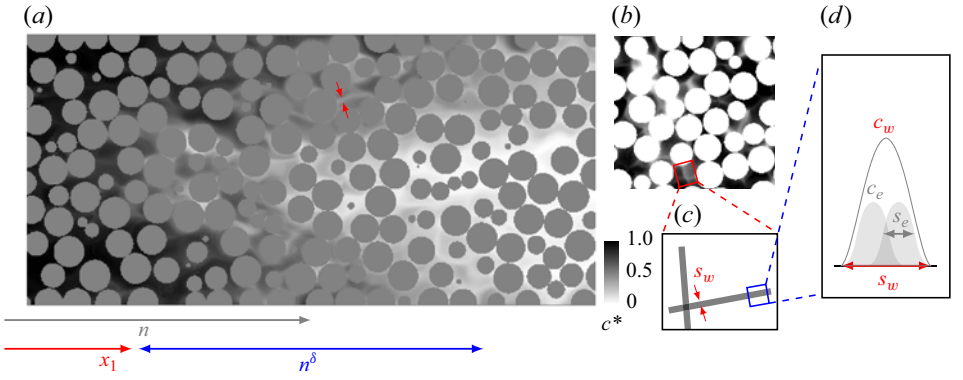


Figure 7. (*a*) Snapshot showing the longitudinal extension n^δ of the dispersive volume, centred at the mean front position $Ut/d = n$. Low-concentration regions (whites) form in particle wakes (red arrows). (*b*) Cross-section showing the sheet-like, three-dimensional structure of white regions (red arrows in panel *a*). (*c*) Magnification of the two overlapping sheets in the red rectangle of panel (*b*). The white sheets, of width s_w, are shown here in grey. (*d*) The observed sheets are bundles of several elementary concentration sheets with maxima c_e and thickness s_e. Bundles have mean thickness s_w and concentration c_w.

The mean concentration front advances as $n = Ut/d$, which also represents the mean number of encountered solid obstacles. White concentration elements accumulate near the mean front, elongating over time and increasing in number from the rear to the head. This leads to a progressive transformation of the initial step profile ($c^* = 1$, $c_w = 0$ at the back; $c^* = 0$, $c_w = 1$ at the head) into a smoother longitudinal profile. The smoothing is the result of longitudinal dispersion, which spreads concentration elements along the streamwise direction.

To quantify the evolution of the concentration front, we compute longitudinal dispersion from the mean square displacement (MSD) of Lagrangian tracers

$$MSD_\ell = \frac{\left\langle [(x_k(t) - x_k(0)) - \langle x_k(t) - x_k(0)\rangle]^2 \right\rangle}{d^2}, \tag{3.10}$$

$$MSD_t = \frac{1}{2d^2}\Big(\left\langle [(y_k(t) - y_k(0)) - \langle y_k(t) - y_k(0)\rangle]^2 \right\rangle + \left\langle [(z_k(t) - z_k(0)) - \langle z_k(t) - z_k(0)\rangle]^2 \right\rangle\Big), \tag{3.11}$$

where MSD_ℓ and MSD_t denote the longitudinal and transverse MSDs, and $(x_k(t), y_k(t), z_k(t))$ are the positions of Lagrangian tracers. After the characteristic flow time $n = 1$, the longitudinal MSD exhibits superdiffusive scaling, while the transverse MSD is diffusive (figure 8).

Longitudinal dispersion spreads tracers along the mean flow direction, producing a dispersive volume whose streamwise length can be also estimated from the Eulerian concentration field. We identify the lowermost position of this volume, x_1, as the first cross-section downstream of which the mean value of c_w remains strictly positive. We then compare the measure of the longitudinal dispersive length estimated from the Eulerian concentration field as $2(n - x_1)$ (see the schematic in figure 7*a*), with the Lagrangian evaluation $\sqrt{MSD_\ell} \propto n^\delta$, where $\delta = 3/4$ is extracted from the superdiffusive trend shown in figure 8. The two measures agree well (figure 8*c*), showing the consistency among simulated Eulerian and Lagrangian data.

https://doi.org/10.1017/jfm.2026.11461 Published online by Cambridge University Press

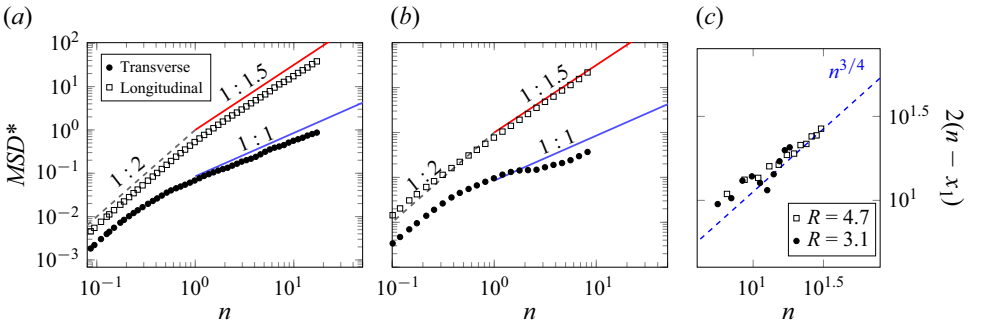


Figure 8. Mean square displacement computed from Lagrangian trajectories (3.11). The longitudinal MSD shows superdiffusive behaviour for (*a*) $R/d = 4.7$ and (*b*) $R/d = 3.1$. (*c*) Comparison between dispersive lengths computed: (i) from Lagrangian statistics, $\sqrt{MSD_\ell}$ (blue dashed line), and (ii) from the Eulerian field, $2(n - x_1)$ (markers), where n and x_1 are the mean and lowermost front positions (see figure 7*a*).

The longitudinal dispersion coefficient thus scales with the mean velocity, $D_\ell \approx Ud$, and the concentration front spreads within a volume whose length increases quasi-linearly in time as n^δ with $\delta \approx 0.75$. At longer times, we expect this superdiffusive regime to transition to Fickian spreading, consistent with observations in anisotropic (Maggiolo *et al.* 2016) and highly heterogeneous media (Souzy *et al.* 2020). The linear $D_\ell - U$ scaling at $Pe = O(10^2)$ is qualitatively in line with previous works, where the longitudinal dispersion coefficient is expected to scale as $D_\ell \propto Pe^{1.19}$ up to $Pe \approx 400$ and transitions to linear scaling at higher Pe (Bijeljic, Muggeridge & Blunt 2004). Transverse dispersion should show a more robust relationship, scaling as $D_t \propto Pe$ (Bijeljic & Blunt 2007); in random packed beds, this behaviour has been experimentally observed at $Pe \gtrapprox 10^3$ (Scheven 2013).

It should be noted that, as an alternative method, longitudinal and transverse dispersion of tracers can be also computed from the velocity distributions via continuous-time random walk theory, which provides relations between Eulerian and Lagrangian velocities for sampling along streamlines. For further reading the reader is referred to Dentz *et al.* (2016).

3.4. *Evolution of pore-scale mixing*

To characterise mixing, we use the concentration variance as a metric for the mixing dynamics. At the pore scale, other common measures include the dilution index (Chiogna *et al.* 2012). The concentration variance is capable of capturing small-scale variability, given sufficient resolution of observation. This can be computed either over a fixed or moving longitudinal region ('fluid supported') or within a subset of that region where the concentration exceeds a threshold ('concentration supported') (Lester *et al.* 2016). In this work, we adopt the fluid-supported variance as the primary mixing metric.

We focus on a subvolume near the mean concentration front, defined by $c^* = 0.5$, that travels along the reactor. In practice, we select a discrete disc of thickness md (with m a constant, chosen between 4 and 6, and d the particle size) such that the volumetric average concentration is $\mu_v = 0.5$. This choice reduces the effect of temporal fluctuations in the mean when computing the variance. The subvolume travels approximately with $n = Ut/d$. To avoid pronounced wall effects (see also panel (*h*) of figure 2), we restrict the area of the disc A to a circle of radius $R - d/2$.

For clarity, we define a shifted streamwise position $x'' = (n - m/2)d$ (see figure 9, right panel), which is the position within the subvolume of length m centred at the mean front

https://doi.org/10.1017/jfm.2026.11461 Published online by Cambridge University Press

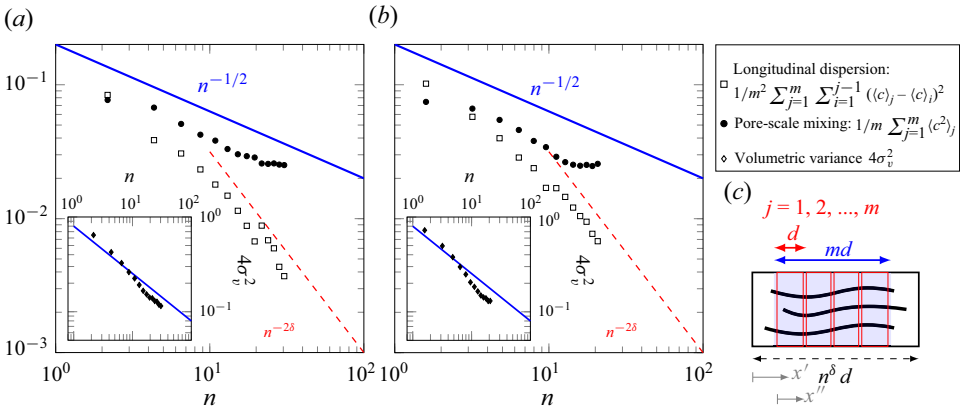


Figure 9. Contributions to the concentration variance σ_v^2 (3.14) for (*a*) $R/d = 4.7$ and (*b*) $R/d = 3.1$ (averaged over two realisations). Longitudinal dispersion (empty squares) decreases in time as $n^{-2\delta}$, while pore-scale mixing (filled circles) decays more slowly $\sim n^{-1/2}$ (solid blue line, (3.27)) and dominates the total variance at long times (insets). Panel (*c*) illustrates the subdivision of the dispersive volume into three-dimensional discs used to compute (3.14).

position n. The volumetric variance in the subvolume is then calculated as

$$\sigma_v^2(t) = \frac{1}{Amd} \int_0^{md} \int_A c^2(\boldsymbol{x}_f, t) \mathrm{d}A \, \mathrm{d}x'' - \mu_v^2(t), \tag{3.12}$$

where $c(\boldsymbol{x}_f, t)$ is the concentration at fluid location $\boldsymbol{x}_f$ and μ_v is its volumetric mean. To separate longitudinal dispersion from pore-scale mixing, we introduce the spatial averaging operator $\langle\ \rangle_j$, applied to a three-dimensional disc of thickness d and area A, centred at $x''/d = (2j-1)/2$, $j = 1, \ldots, m$. Then the first and second moments in (3.12) become

$$\mu_v = \frac{1}{m} \sum_{j=1}^{m} \frac{1}{Ad} \int_{(j-1)d}^{jd} \int_A c(\boldsymbol{x}_f, t) \mathrm{d}A \, \mathrm{d}x'' = \frac{1}{m} \sum_{j=1}^{m} \langle c\rangle_j$$
$$\frac{1}{Amd} \int_0^{md} \int_A c^2(\boldsymbol{x}_f, t) \mathrm{d}A \, \mathrm{d}x'' = \frac{1}{m} \sum_{j=1}^{m} \langle c^2\rangle_j. \tag{3.13}$$

Combining (3.12) and (3.13), the concentration variance can be rewritten as

$$\sigma_v^2(t) = \frac{1}{m^2} \sum_{j=1}^{m} \sum_{i=1}^{j-1} \left(\langle c\rangle_j - \langle c\rangle_i\right)^2 + \frac{1}{m} \sum_{j=1}^{m} \langle c'^2\rangle_j, \tag{3.14}$$

with $c' = c - \langle c\rangle_j$. The first term on the right-hand side quantifies one-dimensional longitudinal dispersion, measuring differences between cross-sectional average concentrations. It scales with the squared longitudinal concentration gradient, $(c_0^*/L_\ell)^2$, where $L_\ell^2 \sim MSD_\ell \propto n^{2\delta}$ (§ 3.3), and thus scales as $n^{-2\delta} \approx n^{-1.5}$ for $\delta \sim 0.75$.

The second term captures transverse variations, measuring pore-scale differences and mixing, with longitudinal pore-to-pore differences removed by computing $\langle\cdot\rangle_j$ over discs of thickness $\lessapprox d$, the characteristic length scale of velocity fluctuations.

Figure 9 shows the evolution of the two contributions to the variance. Longitudinal dispersion reduces concentration differences along the flow direction, scaling as $n^{-2\delta}$

https://doi.org/10.1017/jfm.2026.11461 Published online by Cambridge University Press

(empty squares). Pore-scale mixing decays more slowly (filled circles) and dominates the mixing evolution in the subvolume. This behaviour is important at finite times and will be analysed further in the next sections.

3.5. *Lamellar model in shear flow*

We observe a marked elongation of concentration regions along the streamwise direction and now ask how they form and arrange in space. To address this, we examine the distribution of white concentrations. These low-concentration regions can be regarded as bundles, or aggregates, of several elementary concentration sheets originating from particle wakes. We denote by c_e the maximum concentration of the elementary sheets, and by c_w the maximum concentration within a bundle of mean thickness s_w. A sketch of bundle formation is shown in figure 7, panels (c) and (d).

Each elementary sheet originates in particle wakes and is subsequently deformed by the flow. We can make use of a lamellar model (Villermaux 2019; Dentz *et al.* 2023) to model their evolution under the dominant deformation mechanism at finite times, that is, shear flow. Shear-induced elongation scales as $\Lambda_\ell \propto n^\alpha$, with α extracted from the Lagrangian kinematics in (3.4). The maximum concentration of each sheet after a short mixing time t_m decreases as $c_e = c_0/(s_e n^\alpha)$, with $s_e \propto n^{1/2}$ the transverse size. Since $\alpha \approx 2.25$ exceeds the exponent $\delta \approx 0.75$ of the dispersive volume growth ($n^\alpha > n^\delta$), sheets overlap because of shear deformation at a rate $n^{\alpha-\delta+1/2}$, yielding an effective concentration $c_e n^{\alpha-\delta} s_e$. Overlap is further enforced by their increasing density: since they elongate along the flow direction, the number of elementary sheets per cross-section increases as $n_e = x' n_p$, from dilute ($x' \sim 0$) to dense regions ($x' \sim n$). We emphasise that the density of concentration sheets grows in time since more sheets reach a given longitudinal position.

Aggregation of elementary sheets thus produces bundles (figures 10*c* and 10*f*), and mass conservation at each x' requires

$$\langle c_w \rangle \langle s_w \rangle \frac{n_w}{n_p} = c_e n^{\alpha-\delta} s_e \frac{n_e}{n_p} = \frac{x'}{n^\delta}, \tag{3.15}$$

with $c_0 = 1$ and the symbol $\langle\rangle$ here indicating the sample average per cross-section.

We verify this model numerically, from the pore-scale concentration field. We track the maxima c_w at different cross-sections located within the interval $x_1' = [x_1 : x_1 + (nd))^\delta]$, corresponding to the longitudinal dispersive length centred at the mean front position $Ut/d = n$ (figure 7*a*). The top panels of figure 10 show the sample mean of the maxima $\langle c_w \rangle$ at different dimensionless times n, increasing with the longitudinal position $x' = x_1' - x_1$ within the dispersive volume.

In the dilute region, bundles consist of few sheets and weak aggregation, leading to a power-law decrease of $\langle c_w \rangle$ (figure 10, upper panels) as a result of elongation and diffusion. In the dense region, aggregation dominates and overlap drives $\langle c_w \rangle \to 1$.

Diffusion dilutes the white bundles transversely. The mean lateral spreading $\langle s_w \rangle$ can be inferred from the number of maxima per pore n_w/n_p and their mean separation distance $\langle \ell_w \rangle$, where $n_p = (2R/d)^2$ is the mean number of pores per cross-section. Local maxima arise at intersections of different bundles, and their number per pore is expected to increase with bundle overlap, estimated as $\sim \langle s_w \rangle / \langle \ell_w \rangle$. This leads to

$$\langle s_w \rangle \sim \langle \ell_w \rangle \frac{n_w}{n_p} \propto n^{1/2}, \tag{3.16}$$

implying diffusive growth in time if the elementary sheets expand diffusively as $s_e \propto t^{1/2}$. (In (3.16), ℓ_w and s_w are normalised by the particle size d.) From the middle panels of

https://doi.org/10.1017/jfm.2026.11461 Published online by Cambridge University Press

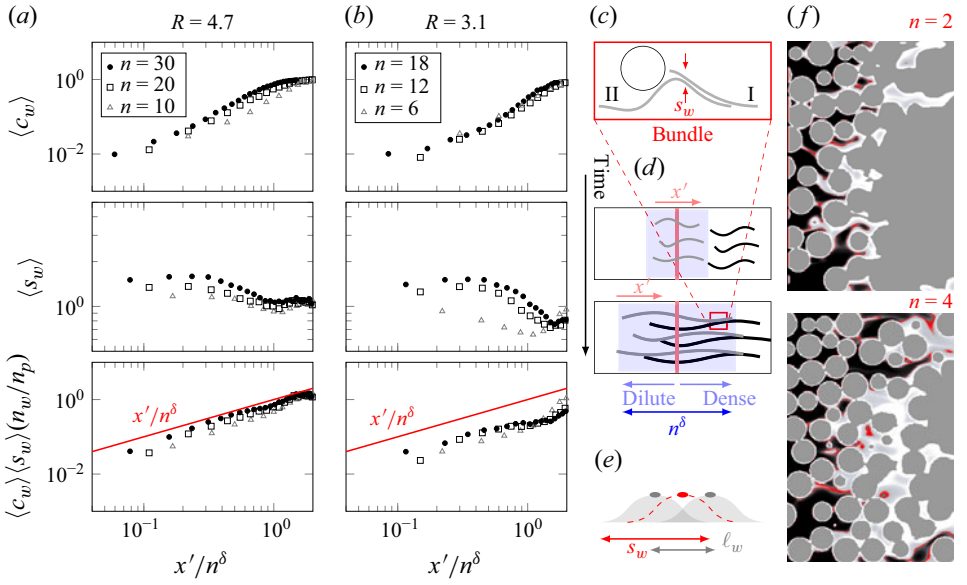


Figure 10. (*a*,*b*) Upper panels: sample mean $\langle c_w \rangle$ per cross-section of the maximum concentrations in white bundles, developing longitudinally along the dispersive volume at different times n, for $R = 4.7$ (*a*) and $R = 3.1$ (*b*). Middle panels: mean lateral bundle size s_w, which grows with n in the dilute region (blue lines). Lower panels: verification of the mass conservation (3.15) (red lines). (*c*) Sketch of elementary sheets of low concentration c_e, elongated longitudinally by the flow (I, II), and overlapping to form bundles of concentration c_w and thickness s_w. (*d*) Bundles are embedded in a dispersive volume of length $\sim n^\delta$ (blue shaded region). Dilute and dense regions of white concentrations are identified upstream and downstream of the mean front position (red vertical line). (*e*) Bundle overlap occurs when the bundle width s_w exceeds their spacing ℓ_w, producing a new maximum (red dot), with $n_w/n_p \sim s_w/\ell_w$. In the rightmost panel (*f*) two snapshots of concentration fields show the emergence of white concentration elementary sheets, forming bundles at downstream positions (top), and later growing in number and merging (bottom).

figure 10 we observe that $\langle s_w \rangle$ increases with n at fixed x', supporting the interpretation of diffusive growth of elementary sheets and subsequent bundle overlap. Finally, in the lowermost panels of figures 10(*a*) and 10(*b*), we also verify (3.15).

Given this satisfactory agreement between the simulations and the lamellar model of deformation in shear flow, we next analyse the mixing dynamics in more detail and provide a more precise prediction through lamellar aggregation. In particular, we focus on the second moments of the concentration maxima, which provide an accurate measure of pore-scale mixing.

3.6. *Aggregation model under shear-induced deformation*

We adopt the shear-flow deformation model (Souzy *et al.* 2018; Villermaux 2019) to describe the dynamics of mixing at finite times. We noted earlier that this model is consistent with the first moments of the white concentration sheets: it is the shear flow together with diffusion that induces the formation of white concentration sheets at the particle wakes and the successive blending at finite times.

We here briefly recall the shear-flow deformation model. At very early times, advection dominates over diffusion, and flow-induced elongation compresses concentration sheets along the transverse direction. As shear-induced deformation is dominant (see § 3.2), the transverse thickness of these white sheets, $s_e(t)$, decreases according to

https://doi.org/10.1017/jfm.2026.11461 Published online by Cambridge University Press

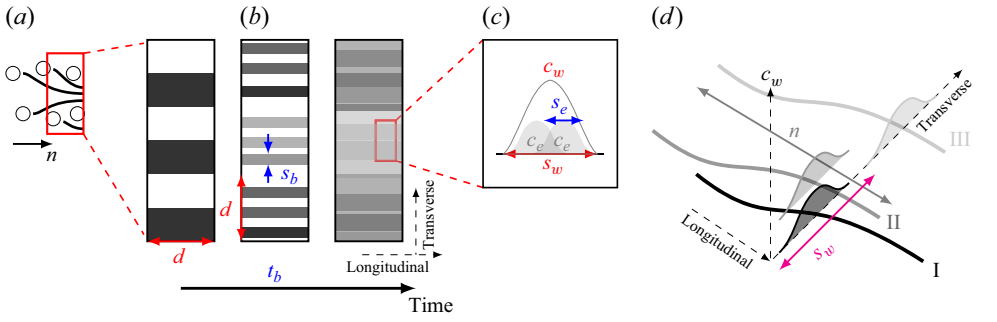


Figure 11. (*a*) At initial times low-concentration sheets emerge from particle wakes because of shear flow. Their initial transverse size is $s_0 = d/2$, so that the total concentration $c^* = 0.5$. (*b*) Schematic illustration of the pore-scale mixing: at the mixing time t_m the sheets have reached their minimum thickness s_b; after the mixing time t_m diffusion merges them, to form bundles of maximum concentration c_w and thickness s_w (*c*). In (*d*) the two modes of overlap are sketched: concentration sheet I overlaps longitudinally with sheet II because of streamwise elongation, while transverse overlap between II and III is sustained by diffusion.

$$s_e^{(1)}(t) \approx s_0(\gamma t)^{-\alpha}, \tag{3.17}$$

where s_0 and $s_0^* = s_0/d$ denote the dimensional and dimensionless initial thickness, respectively.

Applying Ranz's transformation (Ranz 1979) and solving the associated advection–diffusion equation in the transformed Lagrangian frame, one can estimate the characteristic mixing time t_m, at which diffusion ($D/s^2(t)$) begins to counterbalance advection-induced compression ($-(1/s_e)(\mathrm{d}s_e/\mathrm{d}t)$)

$$t_m \sim \frac{1}{\gamma}\left(\gamma^* s_0^{*2} Pe\right)^{1/(2\alpha+1)}, \tag{3.18}$$

where $\gamma = \gamma^* U/d$ is the dimensional shear-induced deformation in three dimensions, as defined in § 3.2. Using the measured $\gamma^* = 5\sqrt{2}$ and $\alpha = 2.25$, we obtain $t_m \approx d/(3U)$.

At this mixing time t_m, elongation and compression yield white concentration sheets with transverse thickness

$$s_b^{(1)} \approx s_0\left(\gamma^* s_0^{*2} Pe\right)^{-\alpha/(2\alpha+1)}, \tag{3.19}$$

which subsequently broadens diffusively as $s_e^{(1)} \sim \sqrt{2Dt}$. These concentration sheets are predominantly elongated along streamlines and thus mainly aligned with the streamwise direction (figure 11, panel *a*).

Up to t_m, in the vicinity of the front, elongation brings together an increasing number of concentration sheets originating from different streamwise positions, while compression prevents their overlap. Beyond t_m, transverse diffusion allows these elements to broaden as $t^{1/2}$, and their maximum concentration decays according to

$$c_e \approx \frac{c_0\, s_0}{(\gamma t)^{\alpha}\sqrt{2Dt}} \propto n^{-(\alpha+1/2)}. \tag{3.20}$$

At this stage, the elements are free to overlap due to the combined effects of shear-induced deformation and transverse diffusion, as schematically illustrated in figure 11. The key positive effect of early-time deformation is that it enhances mixing: by compressing concentration elements transversely, advection brings them closer together, allowing diffusion to merge them more efficiently.

https://doi.org/10.1017/jfm.2026.11461 Published online by Cambridge University Press

We thus define an early-time aggregation model based on shear-induced elongation, the dominant mechanism of deformation at finite times, while exponential stretching dominates at longer times. Under shear-induced deformation, aggregation of white concentration sheets becomes significant at times $t > t_m$ due to two main mechanisms: (i) the mismatch between the longitudinal growth of the sheets and the dispersive volume, occurring at a rate $n^{\alpha-\delta}$, and (ii) the increase in sheet density and reduction in their physical separation, with rate $N(t)$. The increase in physical proximity drives overlap as more longitudinally elongated concentration elements occupy the same pore spaces (figure 6), and transverse diffusion broadens their effective thickness.

The total number of overlaps per pore driven by proximity is estimated as

$$N(t > t_m) \approx (\gamma t)^{\alpha} \sqrt{2Dt}/d \propto n^{\alpha+1/2}, \tag{3.21}$$

which dominates the aggregation dynamics since $N > n^{\alpha-\delta}$. Consequently, the average concentration of aggregates, $c_e N$, remains approximately constant near the front. Mass conservation is also reflected in the first moment of the white bundle maxima, $\langle c_w(x = n)\rangle$, as shown in figure 10. Nevertheless, this constancy does not apply to the variance.

Given that the mean concentration near the front is constant, the random aggregation model of Duplat & Villermaux (2008) can be applied to estimate the variance decay, based on the count of overlapping events among concentration sheets. According to this model, aggregation among decorrelated concentration sheets can be modelled via the random addition of independent and identically distributed variables, or via the sum of the means and variances when they are correlated (Duplat *et al.* 2010). In the former case, one makes use of the central limit theorem, based on the assumption that concentrations within isolated sheets or bundles are identically distributed and picked up randomly when performing aggregation (see also Weiss & Provenzale 2007).

The number of sheets per pore at t_m is the consequence of their early-time elongation beyond a pore space

$$n_b = (\gamma t_m)^{\alpha}, \tag{3.22}$$

which, combined with (3.18) and (3.19), defines the average dimensionless spacing between sheets

$$\ell_b = 1/n_b = s_b/s_0. \tag{3.23}$$

After t_m, sheet overlap occurs via two mechanisms: the persistence of longitudinal, shear-induced elongation (N_ℓ), and transverse diffusion (N_t), so that the total number of overlaps is $N = N_\ell N_t$, as expressed in (3.21)

$$\begin{aligned} N_\ell(t > t_m) &= (\gamma t)^{\alpha} \ell_b, \\ N_t(t > t_m) &= s_e/(\ell_b d) \approx \sqrt{2Dt}/(\mathrm{d}\ell_b). \end{aligned} \tag{3.24}$$

The variance of a single, isolated concentration element is proportional to its squared maximum concentration (Meunier & Villermaux 2010)

$$\sigma_e^2(t) \approx c_e^2 \propto n^{-2\alpha-1}. \tag{3.25}$$

Longitudinal overlap aggregates these elements into bundles (figure 10, panels *c* and *f*). Because shear-induced deformation is correlated over lengths larger than the pore scale d (§ 3.2), the bundle variance can be approximated by the correlated sum of N_ℓ individual variances

$$\sigma_w^2(t) \approx c_{w,max}^2 = N_\ell^2 \sigma_e^2 \propto n^{-1}. \tag{3.26}$$

https://doi.org/10.1017/jfm.2026.11461 Published online by Cambridge University Press

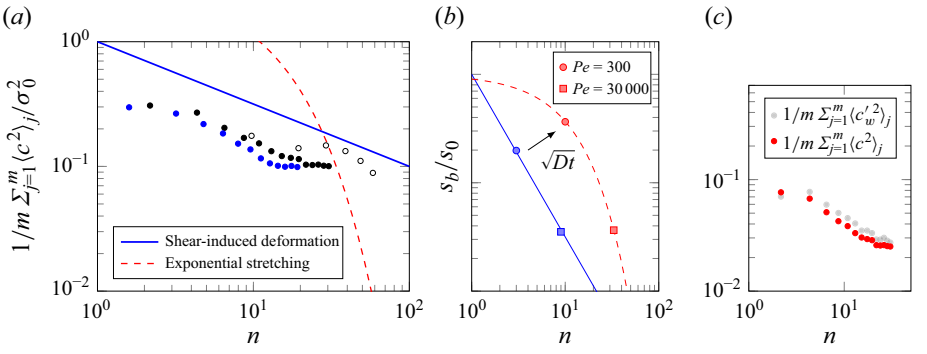


Figure 12. (*a*) Comparison between simulations (black marks: $R/d = 4.7$; blue marks: $R/d = 3.1$), the prediction for random transverse aggregation ((3.27)) and the exponential stretching model (dashed lines). An additional simulation with double reactor length is shown (empty square marks), yet exponential decay is barely observed up to $n \approx 50$. (*b*) Predicted compression of concentration sheets according to (3.17) (blue solid line) and exponential stretching (red dashed line), with markers indicating the thickness reached at the mixing times $s_b^{(1)}$ (blue) and $s_b^{(2)}$ (red) for $Pe = 3 \times 10^2$ and 3×10^4, respectively. (*c*) Verification of volumetric variance and pore-scale mixing term $\sim \langle c^2_{w,max}\rangle$.

In contrast, transverse overlap occurs randomly across the cross-section. Transverse overlap yields values of concentrations that are the sum of different concentrations belonging to bundles interpenetrating with random orientations in the cross-sectional space. This random aggregation rule is justified by the random orientation of azimuthal pore throats, observed in § 3.1, and reported in figure 2. Following this reasoning, the maximum concentrations near the front result from the random addition of N_t values of concentration distributed according to the characteristic PDF of the bundle. Using (3.20) and (3.24), we obtain

$$\sigma^2(t) \approx N_t \sigma_w^2 = N_t N_\ell^2 c_e^2 = B n^{-1/2}, \tag{3.27}$$

where $N_t(t)$ quantifies the evolution of the number of diffusive overlap and B is a constant depending on the initial conditions c_0, s_0, the shear-induced deformation rate γ^* and the Péclet number as

$$B = \frac{c_0^2 s_0}{\sqrt{2}} \left(\frac{s_0^{*2} Pe}{\gamma^{*2\alpha}} \right)^{1/(4\alpha+2)}. \tag{3.28}$$

To better highlight the Pe-dependence one can rewrite (3.27) as

$$\sigma^2(t) \propto (\gamma^* Pe)^{-\alpha/(2\alpha+1)} t^{-1/2}, \tag{3.29}$$

which, in the case of linear shear $\alpha = 1$, yields the same scaling as that proposed for the variance of travel times of species reaching solid surfaces in porous media, as predicted by chaotic restart models (Aquino *et al.* 2023). The present analysis suggests that one can expand such models to account for nonlinear shear and $\alpha \neq 1$.

Numerical results confirm that the variance near the front is well approximated by the variance of bundle maxima, $\sigma^2(t) \sim \langle c_w^2 \rangle$ (figure 12, panel *c*). Evaluating (3.28) with the value of γ^* extracted from Lagrangian deformations (§ 3.2) yields $B \approx 0.2$, which, when substituted into (3.27), provides predictions in good agreement with pore-scale mixing Eulerian data (figure 9, blue solid line vs filled marks, large panels and insets). This confirms that mixing at finite times is dominated by shear-induced deformation.

https://doi.org/10.1017/jfm.2026.11461 Published online by Cambridge University Press

The proposed aggregation model, combining correlated longitudinal and random transverse overlaps, predicts a slower decay of concentration variance than fully three-dimensional random aggregation, where variance scales as $n^{-3/2}$. However, early-time elongation and compression accelerate transverse overlap compared with pure diffusion, leading to variance decay that scales with the mean velocity rather than the molecular diffusion coefficient D, consistent with $n \propto U$.

3.7. *Shear-induced deformation versus exponential stretching*

At longer times, exponential stretching begins to dominate. However, slow shear-induced mixing continues to govern the overall mixing process beyond the characteristic onset time of exponential stretching, i.e. $n \sim 1/\lambda \approx 10$.

During exponential stretching, concentration elements must reach a stable minimum thickness that is independent of the initial concentration Villermaux (2019)

$$s_b^{(2)} \approx d(\lambda Pe)^{-1/2}. \tag{3.30}$$

By inserting the values of the dimensionless shear-induced deformation rate $\gamma^* = \gamma d/U \approx 14$, $\alpha \approx 2.25$ and Lyapunov exponent $\lambda = 0.1$, obtained in § 3.2, into (3.19) and (3.30), we find $s_b^{(1)} < s_b^{(2)}$, since

$$\lambda \ll \gamma^*(\gamma^* s_0^{*2} Pe)^{-1/(2\alpha+1)}. \tag{3.31}$$

In particular, we find $s_b^{(2)} \approx 5 s_b^{(1)}$. This scale separation $s_b^{(1)} < s_b^{(2)}$ holds for moderate Péclet numbers, indicating that concentration elements first reach $s_b^{(1)}$ via shear-induced deformation and subsequently aggregate through diffusion to eventually attain the scale $s_b^{(2)}$ under exponential stretching at later times (provided that the shear induced mixing time t_m, here $t_m = 0.33 d/U$, is smaller than the time for onset of exponential stretching $t_\epsilon = d/(U\lambda)$).

Before being subjected to exponential stretching, the concentration field reorganises through diffusion. To investigate the expected asymptotic behaviour, we performed an additional simulation by doubling the reactor length to $L/d = 84$, which allows the computation of the variance decay up to $n \approx 50$. The results are shown in figure 12. A slight change in the variance decay is observed, hinting at the transition to exponential stretching. However, the limited computational domain prevents a definitive confirmation. For compact, finite-sized porous reactors, where reactions typically occur within $n \approx 10$–50, we conclude that shear-induced deformation remains the dominant mixing mechanism.

It is instructive to compare the observed algebraic decay of variance at early times with experimental observations in similar random packed beds (Heyman *et al.* 2020, 2021), where chaotic flows produce an exponential decay of variance. The Lyapunov exponent ($\lambda \approx 0.17$) and the onset time of chaotic mixing ($t_m^{(2)} \sim 6$) are qualitatively consistent with our findings. However, the early-time algebraic decay is not observed in these experiments. This discrepancy can be attributed to the different injection protocol. We also note that, due to the much higher Péclet numbers – which in those experiments are one to two orders of magnitude greater than in our simulations – the scale separation predicted by (3.31) is greatly reduced, making any possible finite-time shear-deformation less pronounced compared with exponential deformation.

To better highlight the Pe-dependence of the scale separation, we can rewrite (3.31) explicitly in terms of Pe. Then to achieve a relevant difference between $s_b^{(1)}$ and $s_b^{(2)}$,

https://doi.org/10.1017/jfm.2026.11461 Published online by Cambridge University Press

e.g. $s_b^{(2)} > 4s_b^{(1)}$ as in present simulations, the Péclet numbers must satisfy the condition

$$Pe < \frac{\gamma^{*2\alpha}}{s_0^{*2}(4^2\lambda)^{2\alpha+1}}, \tag{3.32}$$

which depends on the shear exponent α. As an example, taking the characteristic pore size $s_0^* = 1$ as initial concentration thickness, $\lambda = 0.1$ and $\gamma^* \approx 10$, for strong nonlinear shear ($\alpha = 2$) we find $Pe < 10^3$ while for linear shear ($\alpha = 1$) we have $Pe < 2\ 10^1$. Equation (3.32) can be interpreted as follows: shear dominates mixing at finite times if the Péclet number is substantially smaller than the ratio between the time scales characterising the onsets of exponential mixing and shear-induced deformations.

3.8. *Mixing with surface reaction*

In the presence of a reactive surface, such as the fluid–catalyst particle interface ($Da_{II} > 0$), the homogenisation of surface concentration and local reaction is governed by the transverse overlap-driven mixing mechanism that determines the scaling of the volumetric variance in (3.27). Indeed, we observe that, for both inert and reactive media, the variance of concentration at the fluid–solid interface, σ_s^2, normalised by the mean μ_s, follows

$$\sigma_s^2/\mu_s^2\ (t < t_k) = An^{-1/2}/\mu_s^2(0) \propto (\gamma^* Pe)^{-\alpha/(2\alpha+1)}(t_D/t)^{1/2}, \tag{3.33}$$

up to the characteristic reaction time $t_k = 1/k_v$ (with $t_D = d^2/D$ a characteristic diffusion time). In the reactive case, we measure slightly higher values, but the temporal trend remains the same. At later times ($t > t_k$), σ_s^2/μ_s^2 appears to saturate for the reactive case (filled marks lower panels of figure 13). This effect is dictated by the local depletion of concentration at the reactive surface, which counterbalances mixing.

Then, by assuming that this mechanism suppresses mixing at the reactive surface for long times, we can make use of (3.33) at time t_k to estimate the variance-mean ratio at long times

$$\sigma_s^2/\mu_s^2(t > t_k) \propto (\gamma^* Pe)^{-\alpha/(2\alpha+1)} {Da_I}^{1/2}, \tag{3.34}$$

which again is consistent with the *Pe*-scaling of second moments of return times in chaotic restart models (Aquino *et al.* 2023), provided one sets $\alpha = 1$. This consistency shows that both random aggregation models and chaotic restart models can in principle capture the heterogeneous distribution of local reactivities at the fluid–solid surface in reactive porous media. Figure 13, panel (*c*), illustrates this comparison for particle sizes $R/d = 3.1$ and $R/d = 4.7$, corresponding to $L/d = 28$ and $L/d = 42$, respectively (see table 1), where $Da_I = 3.33$ and 2.22, respectively. We note that a lower Da_I number (slower reaction) allows more mixing to take effect.

For design purposes, it is useful to highlight that $\sigma_s^2 \propto \mu_s^2 {Da_{II}}^{1/2}(d/L)^{1/2}$ and that surface reaction homogenisation (low σ_s^2) increases with the system length-to-particle-size ratio L/d. Thus, for a given catalyst reaction rate k_v, optimal reactor design should (i) achieve near-complete conversion by maintaining $Da_{II} = k_v L/U = O(1)$, and (ii) promote effective mixing (low σ_s) by either reducing particle size d or proportionally increasing both the flow rate U and reactor length L. In practice, reducing particle size is often challenging due to production constraints and the risk of pore clogging, which limits reactor efficiency. Increasing flow rate and reactor length, on the other hand, offers a more practical strategy – a strategy that we have successfully validated in recent microreactor experiments (Magson *et al.* 2024).

https://doi.org/10.1017/jfm.2026.11461 Published online by Cambridge University Press

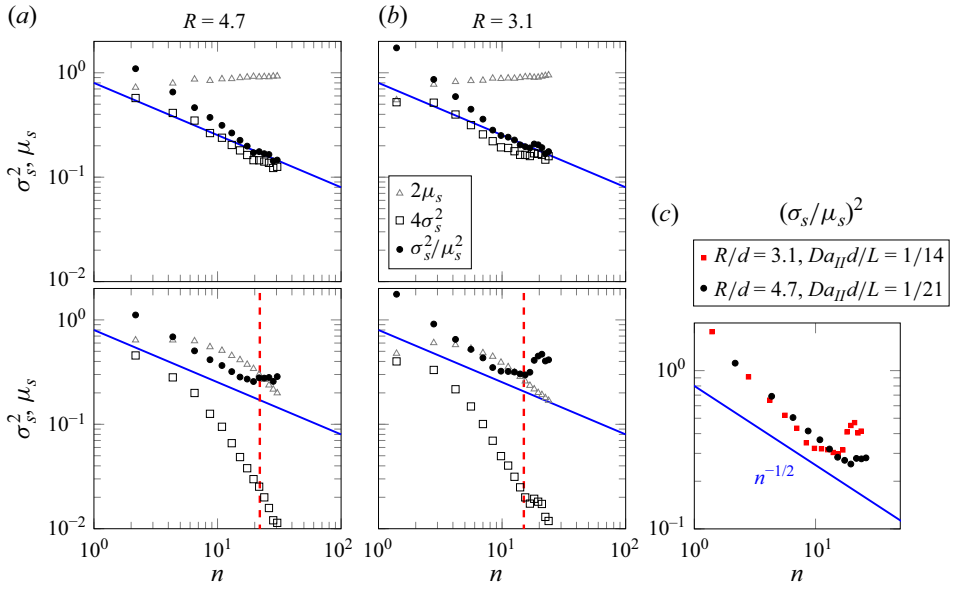


Figure 13. Fluid–solid interfacial concentration mean μ_s and variance σ_s^2 evolution for (*a*) $R/d = 4.7$ and (*b*) $R/d = 3.1$ in inert (top panels) and reactive (lower panels) media. The ratio σ_s^2/μ_s^2 decays similarly, following (3.27) (solid blue lines) in the inert and reactive cases up to the characteristic reactive time $t_k = 1/k$ (vertical red dashed lines in the bottom panels). After t_k the variance-mean ratio at the reactive sites σ_s^2/μ_s^2 saturates. The comparison of σ_s^2/μ_s^2 among the two L/d cases, reported in panel (*c*), shows that, provided the same Da_{II} (see also table 1) mixing is more effective for longer reactors, as predicted by (3.34).

4. Conclusions

In this study, we investigate scalar transport and mixing in porous media at finite times by combining Lagrangian and Eulerian analyses based on a lattice-Boltzmann solver, to unveil the interplay between flow-induced deformation, diffusion and reactive processes. Although the mixing is chaotic, shear-induced deformation can dominate the early-time mixing dynamics, by compressing concentration regions transversely and promoting longitudinal aggregation, which enhances mixing. Transverse diffusion enables overlap between concentration sheets, leading to the formation of partially overlapping lamellar bundles and homogenisation at the pore scale. These mechanisms govern the evolution of both volumetric and surface-concentration variances, producing a characteristic algebraic decay ($\sigma^2 \sim t^{-1/2}$) as verified by numerical simulations. This dynamics is observed when the Péclet number is much smaller than the ratio between the characteristic time scale of exponential mixing and that of shear-induced deformation, a condition that can be satisfied in small, compact fixed-bed reactors.

The aggregation dynamic, which combines correlated longitudinal with random transverse overlaps, explains the slower decay of volumetric variance compared with purely random three-dimensional mixing. This model highlights the critical role of shear-induced deformation in porous media at finite times. Although exponential stretching becomes theoretically relevant at later times, it plays only a secondary role here, because shear-driven mechanisms dominate over the time scales relevant for transport and reaction at moderate Péclet numbers.

In reactive systems, the homogenisation of surface concentrations at fluid–catalyst interfaces mirrors the volumetric mixing trends, with the surface-concentration variance

https://doi.org/10.1017/jfm.2026.11461 Published online by Cambridge University Press

following the same scaling up to the characteristic reaction time. The homogenisation of the surface concentration follows the Pe-scaling $\sigma_s^2 \propto (\gamma^* Pe)^{-\alpha/2(\alpha+1)}$, which enables the extension of shear-induced chaotic restart models (Aquino *et al.* 2023) beyond the linear shear regime ($\alpha = 1$).

In porous systems where the divergence of chaotic trajectories is moderate (Lyapunov exponent $\lambda \approx 0.1$), the Péclet number is moderately high ($Pe = O(10^2)$), and reaction is comparably slow due to molecular diffusion ($Da_I = O(10^1)$), strong shear ($\alpha \approx 2$) can dominate mixing at finite times and control the asymptotic pore-scale surface reaction.

Acknowledgements. We thank the European Union's H2020 research and innovation program under grant agreement no. 951801 (MOST H2020-EIC-FETPROACT-2019-951801). The computations were enabled by resources provided by the National Academic Infrastructure for Supercomputing in Sweden (NAISS), partially funded by the Swedish Research Council through grant agreement no. 2022-06725. The authors thank D. Lester for the fruitful discussion about the computation of the fluid deformation employed in the manuscript.

Declaration of interests. The authors report no conflicts of interest.

Appendix A

The computation of the velocity gradient tensor $\boldsymbol{\epsilon}'(t)$ follows the procedure described in Lester *et al.* (2018). The moving Protean frame $\boldsymbol{x}'$ and the fixed Cartesian frame $\boldsymbol{x}$ are related via the rotation matrix $\boldsymbol{Q}(t)$ as

$$\boldsymbol{x}' = \boldsymbol{x}_0(t) + \boldsymbol{Q}(t)^T \boldsymbol{x}, \tag{A1}$$

with $\boldsymbol{x}_0(t)$ an arbitrary translation vector. The deformation tensor $\boldsymbol{F}(t)$ defines the deformations along a Lagrangian trajectory based on the velocity gradient tensor $\boldsymbol{\epsilon}(t) = \{\nabla \boldsymbol{u}[\boldsymbol{x}(t, \boldsymbol{X})]\}^T$

$$\frac{\mathrm{d}\boldsymbol{F}}{\mathrm{d}t} = \boldsymbol{\epsilon}(t)\boldsymbol{F}(t). \tag{A2}$$

The velocity gradient tensor computed along the Protean frame is

$$\boldsymbol{\epsilon}'(t) = \boldsymbol{Q}(t)^T \boldsymbol{\epsilon}(t) \boldsymbol{Q}(t) + \boldsymbol{A}(t), \tag{A3}$$

composed of two terms, the second of which quantifies the contribution of the moving reference frame

$$\boldsymbol{A}(t) = \frac{\mathrm{d}\boldsymbol{Q}(t)^T}{\mathrm{d}t} \boldsymbol{Q}(t). \tag{A4}$$

By applying the correct transformation (A1) and exploiting the definitions (A3) and (A4), it is possible to render the velocity gradient tensor upper-triangular and redefine (A2) along the Protean frame

$$\frac{\mathrm{d}\boldsymbol{F}'}{\mathrm{d}t} = \boldsymbol{\epsilon}'(t)\boldsymbol{F}'(t), \tag{A5}$$

which is easily solvable for $\boldsymbol{F}'(t)$ with sequential integration, thus allowing the explicit definition of the shear and stretching components determining deformation.

The orientation along the Protean frame is obtained via the rotation matrix $\boldsymbol{Q}(t) = \boldsymbol{Q}_1(t)\boldsymbol{Q}_2(t)$. Given the unit rotation axis $\boldsymbol{q}(t)$ and angle $\theta(t)$

$$\boldsymbol{q}(t) = \frac{1}{\sqrt{v_2^2 + v_3^2}}(0, u_3, -u_2)^T, \tag{A6}$$

https://doi.org/10.1017/jfm.2026.11461 Published online by Cambridge University Press

$$\cos\theta(t) = \frac{u_1}{v}, \tag{A7}$$

where $\boldsymbol{v}(t, \boldsymbol{X}) = (u_1, u_2, u_3)^T$ is the instantaneous velocity of magnitude v along the computed Lagrangian trajectories, the first rotation matrix is defined as

$$\boldsymbol{Q}_1(t) = \cos\theta(t)\boldsymbol{I} + \sin\theta(t)(\boldsymbol{q}(t)_\times)^T + (1 - \cos\theta(t))\boldsymbol{q}(t) \otimes \boldsymbol{q}(t). \tag{A8}$$

In the above (A8), $\boldsymbol{I}$ is the identity matrix, the pedix $\times$ denotes the cross-product matrix while $\otimes$ is the tensor product. The first rotation of the velocity gradient tensor produces the rotated tensor $\boldsymbol{\epsilon}^{(1)}(t)$

$$\boldsymbol{\epsilon}^{(1)}(t) = \boldsymbol{Q}_1(t)^T \boldsymbol{\epsilon}(t) \boldsymbol{Q}_1(t). \tag{A9}$$

The second rotation, applied via $\boldsymbol{Q}_2(t)$, is defined via the angle $\psi(t)$

$$\mathrm{Q}_2(t) = \begin{pmatrix} 0 & 0 & 0 \\ 0 & \cos\psi(t) & -\sin\psi(t) \\ 0 & \sin\psi(t) & \cos\psi(t) \end{pmatrix}. \tag{A10}$$

The final tensor is provided by (A3), which can be rewritten as

$$\boldsymbol{\epsilon}'(t) = \boldsymbol{Q}_2(t)^T \boldsymbol{\epsilon}^{(1)}(t) \boldsymbol{Q}_2(t). \tag{A11}$$

The upper-triangular condition on $\boldsymbol{\epsilon}'(t)$ is enforce by choosing $\psi(t)$ such that it satisfies the following ordinary differential equation:

$$\frac{\mathrm{d}\psi(t)}{\mathrm{d}t} = a(t)\cos^2\psi(t) + b(t)\cos^2\psi(t) + c(t)\cos\psi(t)\sin\psi(t), \tag{A12}$$

where the $a(t)$, $b(t)$ and $c(t)$ coefficients are defined as

$$a(t) = \epsilon^{(1)}_{32} + \frac{u_2}{v + u_1}\epsilon^{(1)}_{31} - \frac{u_3}{v + u_1}\epsilon^{(1)}_{21}, \tag{A13}$$

$$b(t) = \epsilon^{(1)}_{23} + \frac{u_2}{v + u_1}\epsilon^{(1)}_{31} - \frac{u_3}{v + u_1}\epsilon^{(1)}_{21}, \tag{A14}$$

$$c(t) = \epsilon^{(1)}_{22} + \epsilon^{(1)}_{33}, \tag{A15}$$

with $\epsilon^{(1)}_{ij}$ the i, j component of the tensor $\boldsymbol{\epsilon}^{(1)}$. Lester *et al.* (2018) showed that the differential (A12), whilst allowing multiple solutions, admits an attracting trajectory for a specific value of the initial angle condition $\psi(0)$. Such a value can be estimated at short times, via the minimisation of $\mathrm{d}\dot{\psi}/\mathrm{d}\psi$, where $\dot{\psi} = \mathrm{d}\psi/\mathrm{d}t$. Once ψ_0 is identified, the solution of (A12) provides the temporal solution of $\psi(t)$, $\boldsymbol{Q}_2(t)$ along a Lagrangian trajectory. From (A11), the deformation tensor $\boldsymbol{F}'(t)$ can be calculated sequentially as

$$F'_{11} = \frac{v(t)}{v(0)}, \tag{A16}$$

$$F'_{22} = \exp\left[\int_0^t \epsilon'_{22}(t)\,\mathrm{d}t\right], \tag{A17}$$

$$F'_{33} = \exp\left[\int_0^t \epsilon'_{33}(t)\,\mathrm{d}t\right], \tag{A18}$$

$$F'_{12} = v(t)\int_0^t \frac{\epsilon'_{12}(t)F'_{22}(t)}{v(t)}\,\mathrm{d}t, \tag{A19}$$

https://doi.org/10.1017/jfm.2026.11461 Published online by Cambridge University Press

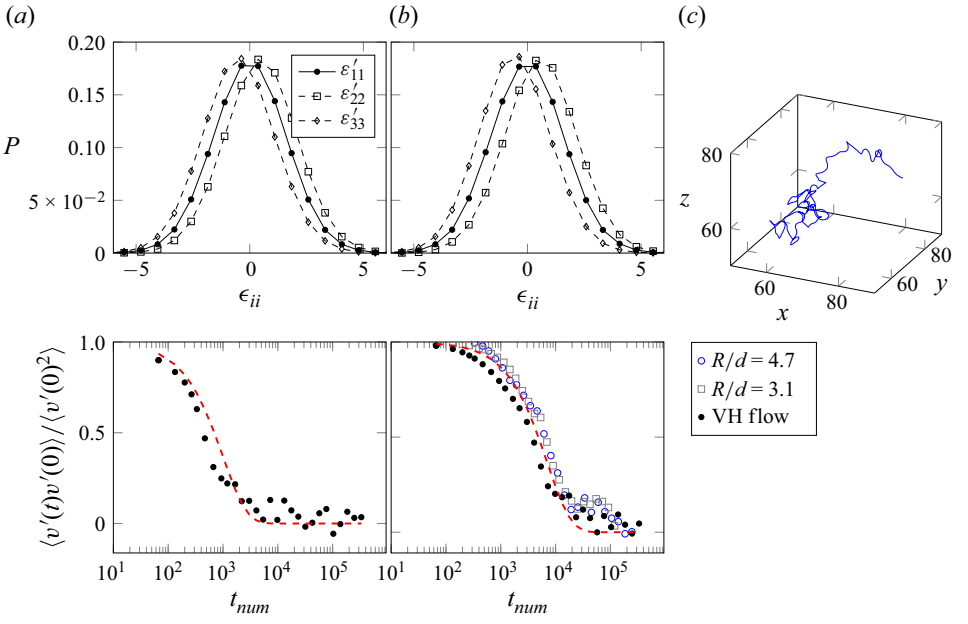


Figure 14. Upper panels: probability distribution functions P of the diagonal components of the velocity gradient tensor ϵ'_{ii} for a characteristic decorrelation time $t'_{num} = 10^3$ (a) and $t'_{num} = 10^4$ (b) for the VH flow. The mean value $\langle \epsilon'_{22} \rangle$ identifies the Lyapunov exponent $\lambda = 0.48$ (a) and $\lambda = 0.57$ (b). Lower panels: velocity autocorrelation function $\langle v'(t)v'(0)\rangle / \langle v'^2(0)\rangle$ (with $v'(t) = v(t) - \langle v(t)\rangle$ the velocity magnitude fluctuation) identifying the decorrelation characteristic time $t'_{num} = 10^3$ (a) and $t'_{num} = 10^4$ (b). The red dashed lines represent the exponential decay $\langle v'(t)v'(0)\rangle / \langle v'^2(0)\rangle = \exp(-t_{num}/t'_{num})$. In the bottom right panel the autocorrelation functions for the reactor simulations $R/d = 4.7$ and $R/d = 3.1$. Right panel (c) shows a trajectory computed on the VH flow.

$$F'_{23} = F'_{22}(t) \int_0^t \frac{\epsilon'_{23}(t) F'_{33}(t)}{F'_{22}(t)} \, \mathrm{d}t, \tag{A20}$$

$$F'_{13} = v(t) \int_0^t \frac{\epsilon'_{12}(t) F'_{23}(t) + \epsilon'_{13}(t) F'_{33}(t)}{v(t)} \, \mathrm{d}t, \tag{A21}$$

We test the procedure described above in the variable helicity (VH) flow as described in Lester *et al.* (2018). The results are shown in figure 14 and a typical trajectory, computed via a Lagrangian tracking algorithm, is presented in the right panel (c). We are particularly interested in the effect of the temporal resolution of trajectory solver on the results accuracy. Once the temporal resolution is chosen, the VH flow supports trajectories that decorrelate over a certain characteristic time t'_{num}, see lower panels in figure 14. We find that to the temporal resolutions $t'_{num} = 10^3$ and $t'_{num} = 10^4$ correspond the mean diagonal components $\langle \epsilon'_{ii} \rangle = (0, 0.48, -0.48)$ and $\langle \epsilon'_{ii} \rangle = (0, 0.57, -0.57)$, respectively. The latter value is not so far from the theoretical maximum of the Lyapunov exponent $\ln(2)$, indicating a good temporal resolution for $t'_{num} = 10^4$. The same resolution is used for the simulations of the trajectories in the reactor, $R/d = 4.7$ and $R/d = 3.1$, as shown in the lower panel (b) of figure 14.

https://doi.org/10.1017/jfm.2026.11461 Published online by Cambridge University Press

References

Aquino, T., Le Borgne, T. & Heyman, J. 2023 Fluid–solid reaction in porous media as a chaotic restart process. *Phys. Rev. Lett.* **130** (26), 264001.

Ben-Noah, I., Hidalgo, J.J. & Dentz, M. 2025 Pore-space partitioning in geological porous media using the curvature of the distance map. *Transp. Porous Med.* **152** (1), 10.

Berkowitz, B., Cortis, A., Dentz, M. & Scher, H. 2006 Modeling non-Fickian transport in geological formations as a continuous time random walk. *Rev. Geophys.* **44** (2), RG2003.

Bijeljic, B. & Blunt, M.J. 2007 Pore-scale modeling of transverse dispersion in porous media. *Water Resour. Res.* **43** (12), W12S11.

Bijeljic, B., Muggeridge, A.H. & Blunt, M.J. 2004 Pore-scale modeling of longitudinal dispersion. *Water Resour. Res.* **40** (11), W11501.

Chiogna, G., Hochstetler, D.L., Bellin, A., Kitanidis, P.K. & Rolle, M. 2012 Mixing, entropy and reactive solute transport. *Geophys. Res. Lett.* **39** (20), L20405.

Dentz, M. & de Barros, F.P.J. 2015 Mixing-scale dependent dispersion for transport in heterogeneous flows. *J. Fluid Mech.* **777**, 178–195.

de Anna, P., Quaife, B., Biros, G. & Juanes, R. 2017 Prediction of the low-velocity distribution from the pore structure in simple porous media. *Phys. Rev. Fluids* **2** (12), 124103.

Dentz, M., Gouze, P. & Carrera, J. 2011 Effective non-local reaction kinetics for transport in physically and chemically heterogeneous media. *J. Contam. Hydrol.* **120**, 222–236.

Dentz, M., Hidalgo, J.J. & Lester, D. 2023 Mixing in porous media: concepts and approaches across scales. *Transp. Porous Med.* **146** (1), 5–53.

Dentz, M., Icardi, M. & Hidalgo, J.J. 2018 Mechanisms of dispersion in a porous medium. *J. Fluid Mech.* **841**, 851–882.

Dentz, M., Kang, P.K., Comolli, A., Le Borgne, T. & Lester, D.R. 2016 Continuous time random walks for the evolution of Lagrangian velocities. *Phys. Rev. Fluids* **1** (7), 074004.

Duplat, J., Jouary, A. & Villermaux, E. 2010 Entanglement rules for random mixtures. *Phys. Rev. Lett.* **105** (3), 034504.

Duplat, J. & Villermaux, E. 2008 Mixing by random stirring in confined mixtures. *J. Fluid Mech.* **617**, 51–86.

Farzaneh, M., Ström, H., Zanini, F., Carmignato, S., Sasic, S. & Maggiolo, D. 2021 Pore-scale transport and two-phase fluid structures in fibrous porous layers: application to fuel cells and beyond. *Transp. Porous Med.* **136** (1), 245–270.

Guo, Z., Zheng, C. & Shi, B. 2002 Discrete lattice effects on the forcing term in the lattice Boltzmann method. *Phys. Rev. E* **65** (4), 046308.

Gurung, D. & Ginn, T.R. 2020 Mixing ratios with age: application to preasymptotic one-dimensional equilibrium bimolecular reactive transport in porous media. *Water Resour. Res.* **56** (7), e2020WR027629.

Heyman, J., Lester, D.R. & Le Borgne, T. 2021 Scalar signatures of chaotic mixing in porous media. *Phys. Rev. Lett.* **126** (3), 034505.

Heyman, J., Lester, D.R., Turuban, R., Méheust, Y. & Le Borgne, T. 2020 Stretching and folding sustain microscale chemical gradients in porous media. *Proc. Natl Acad. Sci. USA* **117** (24), 13359–13365.

Heyman, J., Villermaux, E., Davy, P. & Le Borgne, T. 2024 Mixing as a correlated aggregation process. *J. Fluid Mech.* **992**, A6.

Kree, M. & Villermaux, E. 2017 Scalar mixtures in porous media. *Phys. Rev. Fluids* **2** (10), 104502.

Lester, D., Metcalfe, G. & Rudman, M. 2014 Control mechanisms for the global structure of scalar dispersion in chaotic flows. *Phys. Rev. E* **90** (2), 022908.

Lester, D.R., Dentz, M. & Le Borgne, T. 2016 Chaotic mixing in three-dimensional porous media. *J. Fluid Mech.* **803**, 144–174.

Lester, D.R., Dentz, M., Le Borgne, T. & de Barros, F.P.J. 2018 Fluid deformation in random steady three-dimensional flow. *J. Fluid Mech.* **855**, 770–803.

Lester, D.R., Metcalfe, G. & Trefry, M.G. 2013 Is chaotic advection inherent to porous media flow? *Phys. Rev. Lett.* **111** (17), 174101.

Liang, Y., Yan, S., Tian, P. & Xu, W. 2023 Characterization of solute mixing in heterogeneous media by means of fractal dilution index. *Transp. Porous Med.* **148** (1), 123–135.

Maggiolo, D. 2024 lbdm. Available at: https://gitlab.com/dariom/lbdm.

Maggiolo, D., Modin, O. & Kalagasidis, A.S. 2023 Transition from diffusion to advection controlled contaminant adsorption in saturated chemically heterogeneous porous subsurfaces. *Phys. Rev. Fluids* **8** (2), 024502.

https://doi.org/10.1017/jfm.2026.11461 Published online by Cambridge University Press

MAGGIOLO, D., PICANO, F. & GUARNIERI, M. 2016 Flow and dispersion in anisotropic porous media: a lattice-Boltzmann study. *Phys. Fluids* **28** (10), 102001.

MAGGIOLO, D., PICANO, F., ZANINI, F., CARMIGNATO, S., GUARNIERI, M., SASIC, S. & STRÖM, H. 2020 Solute transport and reaction in porous electrodes at high Schmidt numbers. *J. Fluid Mech.* **896**, A13.

MAGSON, L., MAGGIOLO, D., KALAGASIDIS, A.S., HENNINGER, S., MUNZ, G., KNÄBBELER-BUSS, M., HÖLZEL, H., MOTH-POULSEN, K., FUNES-ARDOIZ, I. & SAMPEDRO, D. 2024 Sustainable heat generation in flow from a molecular solar thermal energy storage system. *Adv. Energy Sustainability Res.* **6**, 2400230.

MEUNIER, P. & VILLERMAUX, E. 2010 The diffusive strip method for scalar mixing in two dimensions. *J. Fluid Mech.* **662**, 134–172.

NISSAN, A. & BERKOWITZ, B. 2018 Inertial effects on flow and transport in heterogeneous porous media. *Phys. Rev. Lett.* **120** (5), 054504.

PRICE, W.S. & SÖDERMAN, O. 2000 Self-diffusion coefficients of some hydrocarbons in water: measurements and scaling relations. *J. Phys. Chem. A* **104** (24), 5892–5894.

RANZ, W.E. 1979 Applications of a stretch model to mixing, diffusion, and reaction in laminar and turbulent flows. *AIChE J.* **25** (1), 41–47.

SCHEVEN, U.M. 2013 Pore-scale mixing and transverse dispersivity of randomly packed monodisperse spheres. *Phys. Rev. Lett.* **110** (21), 214504.

SOLE-MARI, G., BOLSTER, D. & FERNÀNDEZ-GARCIA, D. 2023 A closer look: high-resolution pore-scale simulations of solute transport and mixing through porous media columns. *Transp. Porous Med.* **146**, 85–111.

SOLE-MARI, G., SCHMIDT, M.J., BOLSTER, D. & FERNÀNDEZ-GARCIA, D. 2021 Random-walk modeling of reactive transport in porous media with a reduced-order chemical basis of conservative components. *Water Resour. Res.* **57** (4), e2020WR028679.

SOUZY, M., LHUISSIER, H., MÉHEUST, Y., LE BORGNE, T. & METZGER, B. 2020 Velocity distributions, dispersion and stretching in three-dimensional porous media. *J. Fluid Mech.* **891**, A16.

SOUZY, M., ZAIER, I., LHUISSIER, H., LE BORGNE, T. & METZGER, B. 2018 Mixing lamellae in a shear flow. *J. Fluid Mech.* **838**, R3.

STEWART, R. & ZHANG, H. 2013 A note concerning the distances of uniformly distributed points from the centre of a rectangle. *Bull. Austral. Math. Soc.* **87** (1), 115–119.

TURUBAN, R., LESTER, D.R., HEYMAN, J., BORGNE, T.L. & MÉHEUST, Y. 2019 Chaotic mixing in crystalline granular media. *J. Fluid Mech.* **871**, 562–594.

TURUBAN, R., LESTER, D.R., LE BORGNE, T. & MÉHEUST, Y. 2018 Space-group symmetries generate chaotic fluid advection in crystalline granular media. *Phys. Rev. Lett.* **120** (2), 024501.

VALOCCHI, A.J., BOLSTER, D. & WERTH, C.J. 2019 Mixing-limited reactions in porous media. *Transp. Porous Med.* **130**, 157–182.

VILLERMAUX, E. 2019 Mixing versus stirring. *Annu. Rev. Fluid Mech.* **51**, 245–273.

WANG, Z. et al. 2019 Macroscopic heat release in a molecular solar thermal energy storage system. *Energy Environ. Sci.* **12** (1), 187–193.

WEISS, J.B. & PROVENZALE, A. 2007 *Transport and Mixing in Geophysical Flows*, vol. 744. Springer Science & Business Media.

YANG, G. & WANG, M. 2023 Suitability of body force model for pressure-difference driven flow in porous media. *Comput. Fluids* **265**, 105990.

ZIÓŁKOWSKA, I. & ZIÓŁKOWSKI, D.J.C.E. 1988 Fluid flow inside packed beds. *Chem. Engng Process.: Process Intensification* **23** (3), 137–164.

https://doi.org/10.1017/jfm.2026.11461 Published online by Cambridge University Press